



City Research Online

City St George's, University of London

Citation: Qian, K., Cheng, J., Weng, Y. & Fu, F. (2021). Effect of Loading Methods on Progressive Collapse Behavior of RC Beam-Slab Substructures under Corner Column Removal Scenario. *Journal of Building Engineering*, 44, 103258. doi: 10.1016/j.jobe.2021.103258

This is the accepted version of the paper.

This version of the publication may differ from the final published version. To cite this item please consult the publisher's version.

Permanent repository link: <https://openaccess.city.ac.uk/id/eprint/26719/>

Link to published version: <https://doi.org/10.1016/j.jobe.2021.103258>

Copyright and Reuse: Copyright and Moral Rights remain with the author(s) and/or copyright holders. Copies of full items can be used for personal research or study, educational, or not-for-profit purposes without prior permission or charge, unless otherwise indicated, provided that the authors, title and full bibliographic details are credited, a hyperlink and/or URL is given for the original metadata page and the content is not changed in any way. For full details of reuse please refer to [City Research Online policy](#).

1

Effect of Loading Methods on Progressive Collapse Behavior of RC Beam-Slab

Substructures under Corner Column Removal Scenario

Kai Qian^{1,2*}, Jian-Fei Cheng¹, Yun-Hao Weng¹, Feng Fu³

¹College of Civil Engineering and Architecture, Guangxi University, Nanning, China, 530004.

²College of Civil Engineering and Architecture, Guilin University of Technology, Guilin, China, 541004.

³School of Mathematics, Computer Science and Engineering, City, University of London, U.K, EC1V 0HB.

Abstract: In this paper, high-fidelity finite element (FE) models were developed to investigate the behavior of reinforced concrete (RC) beam-slab substructures to resist progressive collapse under a corner column removal scenario. The numerical models were validated by test results. Then, the validated FE models were employed to investigate the structural behavior under different loading methods, including concentrated loading (CL) and uniformly distributed loading (UDL) methods. Moreover, multi-story frames were built to capture the load redistribution behavior of substructures at different floors under different loading methods. The results indicated that the loading methods affect overall structural responses, load transfer mechanisms, and failure modes. It was demonstrated that the Vierendeel action could not be ignored for multi-story frames to resist progressive collapse caused by the loss of a corner column scenario. More significant Vierendeel action was developed in the structure subjected to CL method than that subjected to UDL method. It was also found that the load transfer mechanisms developed in the top story and bottom story for a multi-story frame are pretty different from those in the middle stories. The bottom story has the most remarkable load resisting capacity.

Keywords: Progressive collapse; Loading method; Load transfer mechanism; Corner column removal.

* Corresponding author. E-mail address: qiankai@glut.edu.cn

23 **1. Introduction**

1
2
24 ASCE/SEI-10 (2010) [1] defines progressive collapse as the spread of an initial local failure from
4
5
25 element to element, eventually resulting in the collapse of the entire structure or a large part of it
7
8
26 disproportionately. Progressive collapse first attracted public attention after the partial collapse of Ronan
10
11
27 Point apartment in London. The research topic became popular after the collapse of Alfred P. Murrah
12
13
14
28 Federal Building in Oklahoma City and World Trade Center in New York. To date, several codes and
15
16
17
29 design guidelines (ASCE/SEI-10 2010 [1]; General Services Administration (GSA) 2003 [2];
18
19
20
30 Department of Defense (DoD) 2009 [3]) had been issued for practical engineers to design buildings in
21
22
23
31 mitigating progressive collapse. There are two main methods commonly suggested by design guidelines:
24
25
26
32 direct and indirect design methods. Due to the uncertainty of extreme events, the alternate load path
27
28
29
33 (ALP) method, one of the direct design methods, has been considered as a major technique as it is event-
30
31
32
34 independent.

34
35 In the past decades, numerous experimental studies [4-18] and numerical simulations [19-25] have
36
37
38 been conducted to investigate the progressive collapse behavior of reinforced concrete (RC) and precast
39
40
41 concrete (PC) structures based on the ALP method. Remarkable efforts have been made towards deeper
42
43
44 understanding of load transfer mechanisms, such as compressive arch action (CAA) [4-6], tensile
45
46
47 catenary action (TCA) [7-9] developed in beams, and compressive membrane action (CMA) [11,12],
48
49
50 tensile membrane action (TMA) in slabs [20,21]. Zhou et al. [4] conducted a series of static tests on a
51
52
53 one-third scaled RC specimen and two PC specimens using dowel bars and corbel to investigate the load
54
55
56 transfer mechanisms of these specimens under a middle column loss. Feng et al. [5] investigated the
57
58
59 progressive collapse behavior of four beam-slab substructures subjected to a corner column loss. It was
60
61
62
63
64
65

44 found that the development of TCA was limited due to weak horizontal constraints from the surrounding
1
245 elements. Sasani [6] investigated the dynamic response of a 6-story RC frame subjected to simultaneous
3
4
546 removal of a corner column and an adjacent exterior column. They concluded that the three-dimensional
6
7
847 Vierendeel action plays a key role in load redistribution. It should be noted that the maximum vertical
9
10
148 displacement was so low that no CAA and TCA were developed. Lu et al. [9] and Ren et al. [10]
12
13
149 conducted several series of laboratory tests on RC specimens with or without slabs. In their tests, both
15
16
50 the middle and edge column removal scenarios were investigated. It was found that the effects of beam
17
18
19
51 height, slab thickness, and seismic reinforcing details dominate the progressive collapse resistance of
20
21
22
52 RC frames.
23
24

253 It should be noted that the majority of existing tests relied on the concentrated loading (CL) method,
26
27
284 which applied a concentrated load on the removed column. However, in reality, the load was uniformly
29
30
3155 distributed on the slab or beam. Thus, the uniformly distributed loading (UDL) method should be applied
32
33
346 to represent real load patterns. However, for UDL method, the weights were increased slowly to simulate
35
36
377 the increment of UDL, which should be very dangerous when reached the ultimate load capacity. In
38
39
58 addition, the softening branch of the load-displacement curve could not be captured. To overcome this
40
41
42
59 drawback, as an alternative method, the multi-points loading method (equivalent UDL), which was a
43
44
45
60 displacement-controlled method, was widely adopted in previous investigations [15-19,21]. Qian et al.
46
47
48
61 [15] carried out a series of RC beam-slab substructures under different column missing scenarios. The
49
50
5162 UDL method was equivalently applied on the slab by a specially designed loading frame. Pham et al.
52
53
543 [17] also adopted the loading tree to equivalently apply UDL on progressive collapse performance of
55
56
5764 beam-slab substructures under the loss of an exterior column scenario. Moreover, flat slab or flat plate
58
59
60
61
62
63
64
65

65 substructures were tested under the equivalent UDL method to investigate the effects of loading methods
1
266 subjected to an interior column removal scenario [16,19].
3
4

57 The effects of loading methods on performance of RC substructures have been explored [18, 21].
6
7
68 The influence of loading methods on the behavior of buildings subjected to the loss of a corner column
9
10
169 is still unclear due to insufficient investigations. Moreover, previous investigation was focused on single-
12
13
1470 story substructures [5,13], which has to ignore the Vierendeel action, one of the important load resisting
15
16
171 mechanisms for RC frames subjected to the loss of a corner column scenario. Thus, in this study, high
18
1972 fidelity finite element (FE) models were developed to quantify the effects of different loading methods
20
21
2273 on the performance of RC frames to resist progressive collapse caused by the loss of a corner column
23
24
2574 scenario. Furthermore, multi-story frames were built to investigate the efficiency of Vierendeel action
26
27
2875 and quantify the mobilization of load transfer mechanisms among different stories with various loading
29
30
3176 methods.
32
33

34 **2. Experimental program and numerical validation** 35 36 37

38 **2.1. Brief of the experimental program** 39 40 41

4279 Before conducting this numerical study, the FE model was validated by the experimental results of
43
44
4580 Feng et al. [5]. The experimental program [5] will be introduced briefly for readers easy to understand
46
47
4881 the validation and FE models. A seismically designed 6-story RC prototype building was designed
49
50
5182 following Chinese codes [26,27], with a height of 3900 mm in the first story and 3600 mm in upper
52
53
5483 stories. The span length in both directions was 5000 mm. The dead load (DL) and live load (LL) were
55
5684 5.5 and 2.0 kPa, respectively. Four 1/2 scaled RC beam-slab substructures were tested subjected to the
57
58
5985 loss of a corner column scenario. However, only the results of Specimen US from Feng et al. [5] were
60
61
62
63
64
65

86 used for validation in this study. The dimensions and reinforcement details of Specimen US are shown
1
37 in Fig. 1. The overall dimension was 3200 mm × 3200 mm. The cross-section of the beam and column
3
4
58 was 100 mm × 250 mm and 300 mm × 300 mm, respectively. The slab thickness was 70 mm. The
6
7
89 transverse reinforcement was bent up 135° and was also installed in the beam-column joints in
9
10
110 accordance with seismic RC detailing. The typical experimental setup and instrumentations are shown
11
12
13
1491 in Fig. 2. Three column supports were fixed to the RC blocks, which were fixed to the strong floor by
15
16
1792 bolts. To simulate the additional constraints from the surrounding slabs, a uniformly distributed load of
18
19
2093 12.0 kN/m² was applied on the extending part of the slab. The load combination of (2DL+0.5LL) is
21
2294 selected, as suggested by GSA 2003 [2]. It should be noted that a one-way pin was installed between the
23
24
2595 hydraulic jack and the top of the corner column stub to allow the corner column stub to rotate and to
26
27
2896 ensure no extra bending will be introduced in the loading process. Thus, Vierendeel action of the frames
29
30
3197 can be neglected in this experimental program. A displacement-controlled CL manner was adopted.

32
33
3498 The average cubic compressive strength of the concrete of Specimen US was 26.6 MPa, which
35
36
3799 corresponded to the cylinder compressive strength of 21.3 MPa. The measured reinforcement properties
38
39
100 are tabulated in Table 1. For detail of test results, please refer to Feng et al. [5].
40
41
42

43 2.2. Numerical model setup 44 45

46
47
48
49
50103 Commercial software LS-DYNA was adopted in this numerical study. Explicit solver was adopted
51
52
53104 to avoid divergence problems. The geometric model of Specimen US is shown in Fig. 3. Similar
54
55
56105 geometric dimensions, reinforcement details, and boundary conditions to the experimental test [5] were
57
58
59
60
61
62
63
64
65

106 2.2.1. *Element types*

1
107 As shown in Fig. 3, both concrete and steel plates were simulated by 8-node solid elements with a
3
4
108 reducing integration scheme. There was one integration point in each solid element, which can
6
7
109 considerably save computational time on the premise of accuracy when hourglass control is
9
10
110 appropriately defined. To ensure the hourglass energy was less than 10% of the total internal energy, the
12
13
111 hourglass coefficient was determined as 0.001. Flanagan-Belytschko stiffness form with exact volume
15
16
112 integration was used. Moreover, reinforcements were modeled using 2-node Hughes-Liu beam elements
17
18
113 with 2×2 Gauss quadrature integration. This beam formulation could effectively simulate the mechanical
20
21
214 property of reinforcements, such as axial force, bi-axial bending, and transverse shear strain.
23
24

25 In this study, sensitivity analysis with three different mesh sizes of 25 mm, 20 mm, and 15 mm are
26
27
286 conducted, as tabulated in Table 2. As shown in Fig. 4, mesh size of 20 mm is adequate, as further mesh
29
30
3117 refinement will not further enhance the accuracy significantly. As a result, the mesh size of concrete
32
33
348 element is chosen as $20 \text{ mm} \times 20 \text{ mm} \times 17.5 \text{ mm}$ for RC slabs and $20 \text{ mm} \times 20 \text{ mm} \times 20 \text{ mm}$ for other
35
36
3719 components. The size of beam element is 20 mm.
38

39 2.2.2. *Material model*

40
41
42 Several constitutive models are available in the material library of LS-DYNA. In this study,
43
44
452 continuous surface cap model (CSCM) is used for concrete as it could effectively simulate the
46
47
483 mechanical property of concrete, including damage-based softening, modulus reduction, shear dilation,
49
50
5124 shear compaction, confinement effect, and strain rate effect [28]. The failure of CSCM model is
52
53
5425 controlled by the shear failure surface and hardening cap surface [29], as shown in Fig. 5. And the yield
55
56
5726 surface is formed based on three stress invariants J_1 , J_2 , and J_3 . Previous studies [19-23] found that
58
59
607 erosion criterion based on the maximum principal strain is a suitable way to simulate concrete crushing
61
62
63
64
65

128 or spalling under both quasi-static and dynamic conditions. However, it could not simulate shear failure
1
129 well when only the maximum principal strain was adopted for the definition of erosion criterion. Thus,
3
4
130 Weng et al. [19] suggested that the maximum principal strain and shear strain criteria should be
6
7
131 considered simultaneously by using keyword *Mat_Add_Erosion. Since the appropriate values are
9
10
132 dependent on the mesh size, the value of maximum principal strain and shear strain is set to 0.08 and 0.3
12
13
133 based on multiple trials. Once the maximum principal strain or shear strain is reached, the solid element
15
16
134 is deleted. Furthermore, the strain rate effect was ignored since only quasi-static behavior was discussed
17
18
135 in this study.
20
21

22 LS-DYNA provides a simplified way to define CSCM (*Mat_CSCM_CONCRETE) for concrete
23
24
237 properties, which only needs three input parameters (unconfined compressive strength f'_c , maximum
26
27
238 aggregate size A_g , and units). Then the remaining material properties are calculated automatically
29
30
3139 according to equations proposed by CEB-FIP concrete model code [30]. But the simplified CSCM is
32
33
340 suited for f'_c between 28 MPa and 58 MPa. Since the unconfined compressive strength f'_c of
35
36
341 Specimens US was 21.3 MPa, the original CSCM (*Mat_CSCM) is used, which requires a series of
38
39
402 input parameters to define concrete material properties, as shown in Table 3.
40
41

42 However, the default concrete material properties would overestimate the initial stiffness and
43
44
424 structural resistance, as shown in Fig. 6. Therefore, a few adjustments on the elasticity modulus and
46
47
445 fracture energy of concrete were made to improve the numerical results. Previous studies [19-21,23]
49
50
5146 suggested that the tensile fracture energy G_{ft} could be reduced to 80% of the default one when it is over
52
53
5447 predicted. If shear or compressive-based damage is significant, the shear fracture energy G_{fs} should be
55
56
548 set as $G_{fs} = 0.5G_{ft}$ and $G_{fc} = 50G_{ft}$. However, the default is $G_{fs} = 100G_{ft}$. In this study, since severe flexural
58
59
609 and torsional failure occurred in the beam ends in Specimen US, both G_{ft} and G_{fs} were adjusted herein.
60
61

150 The detailed parameters of CSCM are listed in Table 3. The unconfined uniaxial stress-strain relationship
1
151 of concrete after adjustments is shown in Fig. 7. The initial stiffness is lower than that of the default one,
3
4
152 and the compressive stress reduces faster in the softening stage. As shown in Fig. 6, the adjusted material
6
7
153 property could improve the numerical results significantly.
9

10
154 The symmetric bilinear elastic-plastic material model (*Mat_Plastic_Kinematic) is used for
12
13
155 reinforcements, which assumes the tensile behavior is identical to that of compressive. The parameters
14
15
16
156 of material properties, including elastic modulus, yield strength, tangential modulus, and ultimate strain,
17
18
19
157 are determined based on the material tests. When the strain exceeds the ultimate elongation ratio, the
20
21
22
158 corresponding reinforcement element is also deleted. The strain rate effect was ignored since only quasi-
23
24
25
159 static behavior was discussed in this study. As suggested by previous works [19,23], a perfect bonding
26
27
28
160 between concrete and reinforcement was assumed based on *Constrained_Lagrange_In_Solid.
29
30

31 2.2.3. *Boundary conditions*

32
33
34
162 In the numerical modeling, similar to the experimental program, the uniformly distributed load was
35
36
37
163 applied on the extending area of the specimen. For simplicity, three concrete blocks were modeled using
38
39
40
164 three rigid plates with zero translations and rotations, as indicated in Fig. 3. Furthermore, a rigid plate
41
42
43
165 was generated at the top of the column stub to prevent stress concentration when concentrated loads
44
45
46
166 were applied. Single surface (*Contact_Automatic_Single_Surface) was defined between the rigid plate
47
48
49
167 and RC column. Besides, static and dynamic coefficients of friction were set as 1.0 at the contact surface
50
51
52
168 to prevent any sliding of the rigid plate. Similar to experimental work, a one-way pin was generated
53
54
55
169 between the loading plate and corner column by using constraint type *Constrained_Joint_Revolute.
56
57
58
59
60
61
62
63
64
65

170 2.3. Validation of the numerical model

1
2
371 Fig. 8 shows the comparison of load-displacement curves between the test results and FE model.
4
5
672 At a large deformation, the TCA in beams and tensile membrane action in slabs is not efficiently
7
8
973 mobilized due to the weak tie force from the surrounding structural members. Thus, the source of load
10
11
1274 resistance is mainly attributed to flexural action or beam action. As shown in Fig. 8, the load-
12
13
1475 displacement curve from FE model is quite similar to test results, including initial stiffness, yield load,
15
16
1776 ultimate load, and ultimate deformation capacity. The error of key results between the FE model and test
18
19
2077 one is less than 7 %, as listed in Table 4.

21
22
2378 It is noted that the crack pattern of the RC beam-slab substructure cannot be directly demonstrated
24
25
2679 because concrete model CSCM is unable to track cracks. However, the cracks can be equivalently
27
28
2980 demonstrated by effective plastic strains. Generally, wider cracks expressed more significant effective
30
31
3281 plastic strains. The concrete damage was quantified through the damage index. Damage index of 0 and
33
34
3582 1 represents no damage and complete failure, respectively. As shown in Figs. 9 and 10, FE model could
36
37
3883 effectively simulate concrete crushing or spalling of the beam and crack patterns of the slab.

39
4084 As a result, the agreement of the load-displacement curves and the failure modes between the
41
42
4385 numerical and test results indicated the validity of the numerical model. Thus, the model was used to
44
45
4686 investigate the load transfer mechanisms of the RC frames with different loading methods and story
47
48
4987 numbers.

50 51 5288 3. Effect of loading methods

53
54
55
5689 Due to the limitation of cost and test conditions, only an experimental study under CL condition
57
58
5990 was conducted by Feng et al. [5]. However, UDL should be applied as gravity load and live load are

191 uniformly distributed along the structure. Thus, it is necessary to study the difference between these two
1
192 loading approaches. As a result, the validated FE model was utilized to evaluate the behavior of RC
3
4
193 beam-slab substructures under both CL and UDL methods.
6
7

194 **3.1. Details of UDL model**

10
11
195 Previous studies [15-19,21] had proved the effectiveness of the 12-point loading tree to simulate
13
14
196 the UDL scheme equivalently. Moreover, Weng et al. [19] modeled the load distribution rig with high
16
17
197 fidelity, and the reliability of the numerical model was proved. Thus, in this study, the same modeling
19
20
198 method was adopted to simulate the behavior of substructures under the UDL method. As shown in Fig.
22
23
199 11, the load distribution rig [19] consisted of a series of rigid beams and plates simulated by 8-node solid
25
26
200 elements. The connection between the top and the secondary rigid beam was defined by keyword
27
28
201 *Constrained_Joint_Revolute [19,21]. The connection between the secondary rigid beam and the
30
31
202 triangle rigid plate was also modeled by keyword *Constrained_Joint_Revolute. The bottom steel plate
33
34
203 was connected with the triangle steel plate by revolute joints to ensure the bottom plates could rotate. In
36
37
204 addition, a contact function was used between the load distribution rig and RC frame by
39
40
205 *Contact_Automatic_Single_Surface [19]. A one-way pin was also defined between the loading plate
42
43
206 and the top rigid beam so that the top rigid beam was able to rotate around the one-way pin. In this study,
45
46
207 each loading point coincided with the centroids of 12 sub-areas, as indicated in Fig. 12.
48

49
208 As shown in Fig. 13, a beam-slab substructure under the UDL method named US-UDL-1F was
51
52
209 built based on the validated model of US-CL-1F. It should be noted that the dimensions, reinforcement
53
54
210 details, and boundary conditions of US-UDL-1F are identical to those of US-CL-1F.
56
57
58
59
60
61
62
63
64
65

211 3.2. Structural resistance

1
2
3 212 Fig. 14 shows the comparison of the load-displacement curves from different loading schemes. As
4
5
6 213 shown in the figure, the peak load of 43.7 kN and 250.6 kN was measured at US-CL-1F and US-UDL-
7
8
9 214 1F, respectively. The initial stiffness, which is defined as the ratio of peak load to the corresponding
10
11
12 215 displacement, of US-CL-1F and US-UDL-1F is 0.52 kN/mm and 5.2 kN/mm, respectively. Thus, the
13
14
15 216 UDL method increases the peak load and initial stiffness by 473% and 897%, respectively. However, it
16
17 217 should be noted that the load capacity from US-UDL-1F should be divided by four before comparing it
18
19
20 218 with US-CL-1F based on a simple load distribution analysis. Thus, as shown in Fig. 14, the load-
21
22
23 219 displacement curve of one-quarter of US-UDL-1F is generally more significant than that of US-CL-1F
24
25
26 220 as the slab deformation of US-UDL-1F is more uniform. No major diagonal crack is formed, and more
27
28
29 221 negative yield lines are observed at the top slab, as shown in Fig. 15.

32 3.3. Load redistribution of beam-slab substructures

33
34
35
36 323 To reveal the difference in load transfer mechanisms of the RC beam-slab substructures with
37
38
39 324 different loading methods, the results of the internal forces of beams and columns were extracted. It
40
41
42 325 should be noted that the beam sections are at a distance of 200 mm away from the beam-column interface
43
44
45 326 to avoid element erosion and fail to provide the internal forces.

47 3.3.1. Development of axial force in beams

48
49
50 328 Fig. 16 shows the development of axial force at the cross-sections near the column stub. Due to
51
52
53 329 symmetry, similar characteristics of axial force development are observed at cross-sections X-beam-1
54
55
56 330 and Y-beam-1. The axial force initially is compressive, indicating the mobilization of CAA. For CL and
57
58
59
60
61
62
63
64
65

231 UDL methods, when the displacement exceeds 370 mm and 296 mm, respectively, the axial force
1
232 transfers into tension, reflecting the development of TCA.
3

4
533 The comparison between Fig. 16 (a) and (b) indicates that the UDL method significantly weakens
6
7
834 the CAA of beams (e.g., the maximum axial compressive force reduces from 198.3 kN to 151.2 kN) but
9
10
135 starts the TCA earlier and greater. For CL and UDL methods, the maximum axial tension force is 38.1
11
12
136 kN and 98.1 kN, respectively, which indicates that TCA is not efficiently mobilized due to fewer
14
15
16
177 constraints from surrounding structural members.
17

18 19 20 **3.3.2. Reactions of supporting columns**

21
229 Figs. 17 (a) and (b) demonstrate the proportion of reaction force at different columns to the total
23
24
250 reaction force under CL and UDL, respectively. For US-CL-1F, at the displacement of 50 mm, 44% and
26
27
281 44% of the load is distributed into columns B and D, respectively. Similarly, at this displacement stage,
29
30
312 42% and 42% of the load are distributed into columns B and D of US-UDL-1F. For US-CL-1F, after
32
33
343 displacement of 82 mm, the proportion of columns B and D decreases with further increasing the
35
36
374 displacement due to concrete crushing occurred at the beam AB and AD. Conversely, the proportion of
38
39
405 column C keeps growing as column C remains almost intact during the test. However, for US-UDL-1F,
41
42
436 after displacement of 20 mm, the proportion of columns B, C, and D nearly maintains constant because
44
45
467 the deformation of the slab and beam is more uniform. In other words, column C suffers more significant
47
48
498 damage when increasing the displacement.
49

50 51 **3.4. Dynamic response**

52
53
54
550 It is worth noting that progressive collapse is normally a dynamic event. Thus, it is necessary to
56
57
581 evaluate the dynamic load capacity of the substructures under different loading methods. Based on
59

252 previous studies [8,14,15,22], an energy-based model, which was proposed by Izzuddin et al. [31], was
 1
 253 adopted in this dynamic evaluation. The dynamic resistance of the specimens could be determined by
 3
 4
 254 Eq. (1).

$$P_d(u_d) = \frac{1}{u_d} \int_0^{u_d} P_{NS}(u) \epsilon \quad (1)$$

256 where $P_d(u)$ and $P_{NS}(u)$ represent the dynamic load resisting function and nonlinear static load
 13
 14
 257 resisting function, respectively.

258 Fig. 18 illustrates the dynamic behavior of the beam-slab substructures. The dynamic peak loads of
 19
 20
 259 US-CL-1F and US-UDL-1F are 36.9 and 224.4 kN, respectively. Similar to the conclusions from
 22
 23
 260 nonlinear quasi-static results, the UDL method could increase the dynamic peak load by 508%. Even,
 25
 26
 261 the load resistance of US-UDL-1F is divided by four, the UDL method could increase the dynamic load
 28
 29
 262 capacity of CL-case by 52 %.

263 4. Analysis of multi-story frame structures

264 Progressive collapse is a global behavior for a multi-story building. However, only a single-story
 38
 39
 265 beam-slab substructure was tested in the test program [5]. Thus, it is imperative to understand whether
 40
 41
 266 the load transfer mechanisms in the single-story substructure are the same as those in a multi-story
 43
 44
 267 building. As shown in Fig. 19, US-CL-2F and US-UDL-2F were established, which represent a two-
 46
 47
 268 story frame substructure under CL and UDL methods, respectively. It should be noted that the load
 49
 50
 269 distribution tree, similar to US-UDL-1F, was generated in each story of US-UDL-2F.

270 **4.1. The role of Vierendeel action**

1
2
271 As concluded by Sasani [6], in moment frames, Vierendeel action is the major mechanism for the
4
5
272 load redistribution of RC frames subjected to the loss of a corner column scenario. The Vierendeel action
7
8
273 could resist the collapse of the buildings. For simplicity, due to the Vierendeel action, bending moment
10
11
274 may develop in the beam end near the corner column to help the resistance of collapse.
12
13

14
15 Fig. 20 demonstrates the comparison of load resistance between single-story and two-story moment
16
17
176 frames under both CL and UDL methods. The peak load of US-CL-1F, US-CL-2F, US-UDL-1F, and
18
19
20
207 US-UDL-2F are 43.7 kN, 250.6 kN, 141.9 kN, and 525.2 kN, respectively. Thus, for CL method, the
21
22
23
238 peak load of US-CL-2F is 324 % of that of US-CL-1F, which is much greater than the theoretical value
24
25
26
269 of 200 %. The relatively large discrepancy could be attributed to Vierendeel action developed in US-
27
28
280 CL-2F. For US-CL-1F, no Vierendeel action could be developed as the constraints from structural
29
30
31
32 components in the upper story are ignored. However, the peak load of US-UDL-2F is 210 % of that of
33
34
35
36
37
38
383 mentioned above, the effects of Vierendeel action are expressed by developing positive moment at the
39
40
404 beam end near the corner column. Thus, the mobilization of Vierendeel action may be reflected
41
42
43
435 indirectly by the magnitude of shear force developed in the corner column. As shown in Fig. 21, much
44
45
46
466 greater shear force develops in the corner column of US-CL-2F, comparing to US-UDL-2F.
47
48

49
50 **4.2. Structural resistance from each story**

51
52
53
538 Fig. 22 shows the comparison of the load resistance from different stories of a two-story frame with
54
55
56
569 that from a single-story substructure. As shown in the figure, the load resistance of each story is different
57
58
590 after the elastic stage. For CL method, compared with the single-story frame, the peak load of the first
60
61
62
63
64
65

291 and second stories increases by 79 % and 58 %, respectively. However, under the UDL condition, the
1
292 peak load of the first and second stories only increases by 7 % and 3 %, respectively. For both loading
3
4
293 approaches, the bottom story achieves the greater load resisting capacity, which indicates that the
6
7
294 Vierendeel action is more efficient in the bottom story, as the structural components in the second story
9
10
295 could provide more significant constraints to the corner joint in the bottom story.
12
13

14 **4.3. Load transfer mechanisms of multi-story RC frames** 15

17
18 As aforementioned, the load transfer mechanisms in each story of the two-story frame are different.
19
20
298 Thus, it is necessary to investigate load transfer mechanisms developing in each story of multi-story
22
23
299 frames. Note that US-CL-3F, US-CL-4F, and US-CL-5F represent three-story, four-story, and five-story
25
26
300 frame substructures under CL case, respectively. Similarly, US-UDL-3F and US-UDL-4F represent
27
28
301 three-story and four-story frame substructures under the UDL case.
30
31

32 **4.3.1. Structural resistance of multi-story frames** 33

34
35 For US-CL-3F、US-CL-4F, and US-CL-5F, as shown in Fig. 23 (a), (b), and (c), the structural
36
37
384 resistance developing in each story is different. The maximum load resistance is observed in the first
39
40
405 story, which is the same as that found in US-CL-2F. By increasing the number of stories, it can be found
42
43
406 that the initial stiffness, peak load, and residual load resistance of the middle story are pretty similar,
45
46
407 which indicates that the development of load transfer mechanisms of the middle stories is almost
48
49
308 identical. Moreover, the peak load of the middle stories is the least compared with the top and bottom
50
51
509 ones. Like the CL case, for US-UDL-3F and US-UDL-4F, as shown in Fig. 24 (a) and (b), the bottom
53
54
5510 story also achieves the most significant initial stiffness and peak load. However, the difference of load
56
57
581 resistance between the top story and the middle story is quite limited due to less Vierendeel action
59
60
61
62
63
64
65

312 developed in UDL cases. In addition, due to the weak tie force from the surrounding elements, less TCA
1
313 and TMA could be mobilized to resist progressive collapse under both CL and UDL methods. As shown
3
4
314 in Fig. 23, comparing the load-displacement curve of the first story in models of US-CL-3F, US-CL-4F,
6
7
315 and US-CL-5F shows that increasing the story number will not affect the load resistance and load transfer
9
10
316 mechanisms of the first story. In other words, the constraints to the corner joint in the first story are
12
13
317 similar whatever the story number is three, four, or five.
14
15

318 **4.3.2. Axial force of beams in multi-story frames**

17
18

19 Similar to what was discussed in section 3.3, the results of axial force in beams were also extracted
20
21
22 to illustrate the load transfer mechanisms. For simplicity, only the cross-sections of beam AB were
23
24
25 discussed herein. Note that the label of X-beam-1 to X-beam-5 represents the beams in the first to the
26
27
28 fifth story, respectively.
29
30

31 As shown in Fig. 25, for CL case, the beams in each story are in compression before the
32
33
34 displacement of 300 mm. After that, the axial force starts to decrease and changes into tension
35
36
37 successively. Moreover, the beams in the first story begin to develop the CAA initially and achieve the
38
39
40 maximum compressive force of 209.6 kN at the displacement of 112 mm. By contrast, beams in the top
41
42
43 story achieve the maximum compressive force of 128.7 kN at the displacement of 214 mm, which
44
45
46 indicates lower CAA developed in top story. Moreover, the compressive force is the least in the middle
47
48
49 story compared with the top and first stories. Similarly, for UDL case, as shown in Fig. 26, the largest
50
51
52 compressive force of 106.3 kN is measured in the first story. Moreover, the compressive force in the
53
54
55 beams in the top story is slightly larger than that in the middle story.
56

57 For both loading methods, it is observed that the axial force of beams in the middle stories is similar,
58
59
60 which agrees well with the results of load resistance.
61
62
63
64
65

334 5. Conclusions

1
2
335 Based on the numerical and parametric study conducted in this study, the following conclusions are
4
5
336 drawn:

337 1. Compared with experimental results, it is found that the high-fidelity numerical models can simulate
10
11
338 the global behavior of the RC beam-slab substructure subjected to a corner column loss scenario well.

12
13
14
339 However, the shear fracture energy should be adjusted to well simulate the stiffness of the concrete in
15
16
340 CSCM.

17
18
19
20
21
341 2. For single-story models under either UDL or CL methods: US-UDL-1F and US-CL-1F, the peak
22
23
342 load of US-UDL-1F is 537 % of that US-CL-1F, which is greater than the theoretical value of 400%.

24
25
26
343 Thus, it indicates that the simplified CL method may underestimate the load resistance of the beam-slab
27
28
29
344 substructures subjected to the loss of a corner column scenario. It could be explained as UDL method
30
31
345 may achieve more uniform deformation of the beam and slab, and thus, more materials could be fully
32
33
34
346 mobilized.

35
36
37
38
347 3. For multi-story models, it was found that Vierendeel action could not be ignored to resist
39
40
41
348 progressive collapse of RC frames caused by the loss of a corner column scenario. Comparing to multi-

42
43
44
349 story frames subjected to UDL method, the Vierendeel action has more significant effects on the frames
45
46
350 under CL method. As the building was subjected to UDL load, in reality, the commonly used CL method

47
48
49
351 may overestimate the contribution of Vierendeel action. Moreover, the Vierendeel action is more
50
51
352 efficient in lower stories than that in the upper stories. Therefore, in practical design, it was suggested

52
53
353 to apply UDL load and generating multi-story frames to obtain more accurate results.
54
55
56
57
58
354 4. The numerical results indicated that the load transfer mechanisms developed in different stories are

355 not identical for a multi-story frame subjected to the loss of a corner column scenario. Moreover, it was
1
356 found that increasing the story number will not affect the load resistance and load transfer mechanism
3
4
357 of the first story.
6
7

358 **References**

- 10
359 [1] ASCE/SEI 7, Recommendations for Designing Collapse-Resistant Structures, Structural
12
13
360 Engineering Institute-American Society of Civil Engineers, Reston, VA, 2010.
15
16
361 [2] GSA, Progressive Collapse Analysis and Design Guidelines for New Federal Office Buildings and
18
19
362 Major Modernization Projects, U.S. General Service Administration, Washington, DC, 2003.
21
22
363 [3] Department of Defense (DoD), Design of Building to Resist Progressive Collapse. Unified Facility
24
25
364 Criteria, UFC 4-023-03, US Department of Defense, Washington (DC), 2009.
28
365 [4] Y. Zhou, T.P. Chen, Y.L. Pei, H.J. Hwang, X. Hu, W.J. Yi, L. Deng, Static load test on progressive
30
31
366 collapse resistance of fully assembled precast concrete frame structure, Eng. Struct. 200 (2019) 109719.
32
33
367 [5] P. Feng, H.L. Qiang, X. Ou, W.H. Qin, J.X. Yang, Progressive collapse resistance of GFRP-
35
36
368 strengthened RC beam–slab subassemblages in a corner column–removal scenario, J. Compos. Constr.
38
39
369 23 (2018) 04018076.
41
42
370 [6] M. Sasani, Response of a reinforced concrete infilled-frame structure to removal of two adjacent
44
45
371 columns, Eng. Struct. 30(9) (2008) 2478-2491.
47
48
372 [7] K. Qian, S.L. Liang, F. Fu, Y. Li, Progressive collapse resistance of emulative precast concrete
50
51
373 frames with various reinforcing details, J. Struct. Eng. 147(8) (2021) 04021107.
52
53
374 [8] X.F. Deng, S.L. Liang, F. Fu, K. Qian, Effects of high-strength concrete on progressive collapse
55
56
375 resistance of reinforced concrete frame, J. Struct. Eng. 146(6) (2020) 04020078.
58
59
376 [9] X.Z. Lu, K.Q. Lin, Y. Li, H. Guan, P.Q. Ren, Y.L. Zhou, Experimental investigation of RC beam-

- 377 slab substructures against progressive collapse subject to an edge-column-removal scenario, Eng. Struct.
1
378 149 (2017) 91-103.
3
4
- 379 [10]P.Q. Ren, Y. Li, X.Z. Lu, H. Guan, Y.L. Zhou, Experimental investigation of progressive collapse
6
7
380 resistance of one-way reinforced concrete beam-slab substructures under a middle-column-removal
9
10
381 scenario, Eng. Struct. 118 (2016) 28-40.
12
13
- 382 [11]N.S. Lim, K.H. Tan, C.K. Lee, Experimental studies of 3D RC substructures under exterior and
14
15
383 corner column removal scenarios, Eng. Struct. 150 (2017) 409–427.
17
18
- 384 [12]A.T. Pham, N.S. Lim, K.H. Tan, Investigations of tensile membrane action in beam-slab systems
20
21
385 under progressive collapse subject to different loading configurations and boundary conditions, Eng.
23
24
386 Struct. 150 (2017) 520–536.
26
27
- 387 [13]K. Qian, B. Li, Slab effects on response of reinforced concrete substructures after loss of corner
29
30
388 column, ACI Struct. J. 109 (6) (2012) 845–855.
32
33
- 389 [14]K. Qian, B. Li, J.X. Ma, Load-carrying mechanism to resist progressive collapse of RC buildings,
35
36
390 J. Struct. Eng. 141(2) (2015) 04014107.
37
38
- 391 [15]K. Qian, B. Li, Z. Zhang, Influence of multicolumn removal on the behavior of RC floors, J. Struct.
40
41
392 Eng. 142 (5) (2016), 04016006.
43
44
- 393 [16]K. Qian, B. Li, Load-resisting mechanism to mitigate progressive collapse of flat slab structures,
46
47
394 Mag. Concr. Res. 67 (7) (2015) 349–363.
49
50
- 395 [17]P.X. Pham, K.H. Tan, Experimental response of beam-slab substructures subject to penultimate-
52
53
396 external column removal, J. Struct. Eng. 141(7) (2015) 04014107.
55
56
- 397 [18]X.D. Pham, K.H. Tan, Experimental study of beam–slab substructures subjected to a penultimate-
58
59
398 internal column loss, Eng. Struct. 55 (2013) 2–15.
60
61
62
63
64
65

- 399 [19] Y.H. Weng, K. Qian, F. Fu, Q. Fang, Numerical investigation on load redistribution capacity of flat
1 slab substructures to resist progressive collapse, *J. Build. Eng.* 29 (2020) 101109.
400
3
4
- 401 [20] K. Qian, Y.H. Weng, F. Fu, X.F. Deng, Numerical evaluation of the reliability of using single-story
6 substructures to study progressive collapse behaviour of multi-story RC frames, *J. Build. Eng.* 33 (2021)
7
402 101636.
9
10
403
- 404 [21] J. Yu, L. Luo, Y. Li, Numerical study of progressive collapse resistance of RC beam-slab
14 substructures under perimeter column removal scenarios, *Eng. Struct.* 159 (2018) 14-27.
15
16
405
17
- 406 [22] A.T. Pham, K.H. Tan, J. Yu, Numerical investigations on static and dynamic responses of reinforced
20 concrete sub-assemblages under progressive collapse, *Eng. Struct.* 149 (2017) 2-20.
21
407
23
24
- 408 [23] J. Yu, Y.P. Gan, J. Wu, H. Wu, Effect of concrete masonry infill walls on progressive collapse
26 performance of reinforced concrete infilled frames, *Eng. Struct.* 191 (2019) 179-193.
27
409
29
30
- 410 [24] Y. Li, X.Z. Lu, H. Guan, L.P. Ye, An improved tie force method for progressive collapse resistance
32 design of reinforced concrete frame structures. *Eng. Struct.* 33(10) (2011) 2931–2942.
33
411
35
36
- 412 [25] D.C. Feng, S.C. Xie, J. Xu, K. Qian, Robustness quantification of reinforced concrete structures
37 subjected to progressive collapse via the probability density evolution method, *Eng. Struct.* 202 (2020)
38
413
40
41
42
414 109877.
43
44
- 415 [26] Ministry of Housing and Urban-Rural Development of the People's Republic of China (MOHURD).
46 Code for design of concrete structures. GB50010-2010. Beijing, China; 2010.
47
48
49
50
- 416 [27] Ministry of Housing and Urban-Rural Development of the People's Republic of China (MOHURD).
51 Code for seismic design of buildings, GB50011-2010. Beijing, China; 2010.
52
53
418
55
56
- 419 [28] Y. Wu, J.E. Crawford, J.M. Magallanes, Performance of LS-DYNA concrete constitutive models,
58 12th Int. LS-DYNA Users Conf, Livermore Software Technology Corporation, Livermore, CA, 2012.
59
420
60
61
62
63
64
65

421 [29]J. Hallquist, LS-DYNA Keyword User’s Manual, Version 971, Livermore Software Technology
1
422 Corp., Livermore, CA, 2007.
3

4 [30]CEB. CEB-FIP model code 1990. Thomas Telford; 1991.
6

7
424 [31]B.A Izzuddin, A.G Vlassis, A.Y Elghazouli, D.A Nethercot, Progressive collapse of multi-storey
9
10 buildings due to sudden column loss — Part I: Simplified assessment framework, Eng. Struct. 30(5)
425
11
12 (2008) 1309–18.
13
426
14
15

427
16

17 **Captions of tables**

18

19
20
429 **Table 1**-Reinforcement properties
22

23
430 **Table 2**-Study on different mesh sizes
24

25
26
431 **Table 3**-Model parameters of CSCM for FE models (Unit: N, mm and ms)
27

28
29
432 **Table 4**-Comparison of key results between test and FE model
30

31

32

33

34

35 **Captions of figures**

36

37

38 **Fig. 1**–Dimensions of specimen US (units: mm) [5]
39

40

436 **Fig. 2**–Test setup and instrumentation location in the referenced experiment [5]
42

43

44 **Fig. 3**–Numerical model of US-CL-1F
45

46

47 **Fig. 4**–Comparison of different mesh sizes
48

49

439 **Fig. 5**–General shape of concrete model yield surface
50

51

52 **Fig. 6**–Comparison of different concrete input parameters
440
53

54

55 **Fig. 7**–Unconfined uniaxial stress-strain curve of concrete based on CSCM
441
56

57

58 **Fig. 8**–Comparison of load-displacement curves between test and FE model
442
59

60

61

62

63

64

65

- 443 **Fig. 9**–Comparison of failure modes between test and FE model: (a) US [5]; (b) US-CL-1F
 1
 444 **Fig. 10**–Comparison of the crack distributions between test and FE model: (a) US [5]; (b) US-CL-1F
 3
 4
 445 **Fig. 11**–Details of numerical model for load distribution rig
 6
 7
 446 **Fig. 12**–Layout of the loading system (unit: mm)
 9
 10
 447 **Fig. 13**–Numerical model of US-UDL-1F
 11
 12
 448 **Fig. 14**–Comparison of load-displacement curves between US-CL-1F and US-UDL-1F
 14
 15
 449 **Fig. 15**–Failure modes of the slab in model US-UDL-1F: (a) Top surface of the slab; (b) Bottom surface
 17
 18
 450 of the slab
 20
 21
 451 **Fig. 16**–Development of beam axial force: (a) US-CL-1F; (b) US-UDL-1F
 23
 24
 452 **Fig. 17**–Contribution of each supporting column: (a) US-CL-1F; (b) US-UDL-1F
 26
 27
 453 **Fig. 18**–Dynamic resistance of beam-slab substructures
 29
 30
 454 **Fig. 19**–Numerical models: (a) US-CL-2F; (b) US-UDL-2F
 32
 33
 455 **Fig. 20**–Comparison of load-displacement curves between CL and UDL conditions
 35
 36
 456 **Fig. 21**–Development of shear force of corner column
 37
 38
 457 **Fig. 22**–Comparison of load resistance from different stories with single-story substructure: (a) US-CL-
 40
 41
 458 2F; (b) US-UDL-2F
 43
 44
 459 **Fig. 23**–Load resistance of each story under CL: (a) US-CL-3F; (b) US-CL-4F; (c) US-CL-5F
 46
 47
 460 **Fig. 24**–Load resistance of each story under UDL: (a) US-UDL-3F; (b) US-UDL-4F
 49
 50
 461 **Fig. 25**–Beam axial force of each story under CL: (a) US-CL-3F; (b) US-CL-4F; (c) US-CL-5F
 52
 53
 462 **Fig. 26**–Beam axial force of each story under UDL: (a) US-UDL-3F; (b) US-UDL-4F
 55
 56
 57
 58
 59
 60
 61
 62
 63
 64
 65

Table 1-Reinforcement properties

Items	Diameter (mm)	Yield strength (MPa)	Ultimate strength (MPa)	Elongation (%)	Yield strain ($\mu\epsilon$)
R6	6	324	525	23	1543
T12	12	427	530	18	2135

Note: R6 represents plain bar with diameter of 6 mm; T12 represents deformed rebar with diameter of 12 mm.

Table 2-Study on different mesh sizes

Type	Mesh size 1	Mesh size 2	Mesh size 3
Mesh size of slabs (mm)	25×25×23.3	20×20×17.5	20×20×14
Mesh size of beams and columns (mm)	25×25×25	20×20×20	15×15×15
Mesh size of Reinforcements (mm)	25	20	15
Total number of solid elements	76672	152325	367990
Total number of beam elements	23330	29210	38708
Time consuming (s)	36241	43717	144940

Table 3-Model parameters of CSCM for FE models (Unit: N, mm and ms)

MID	RO	NPLOT	INCRE	IRATE	ERODE	RECOV	ITRETRE
1	0.00232	1	0.0	0	1.10	0.0	0
PRED							
0.0							
G	K	ALPHA	THETA	LAMDA	BETA	HN	CH
5000	5476	13.408	0.2751	10.5	0.01929	0.0	0.0
ALPHA1	THETA1	LAMDA1	BETA1	ALPHA2	THETA2	LAMDA2	BETA2
0.74735	0.001315	0.17	0.07639	0.66	0.001581	0.16	0.07639
R	XD	W	D1	D2			
5.0	87.8	0.05	2.5e-4	3.492e-7			
B	GFC	D	GFT	GFS	PWRC	PWRT	PMOD
100.0	3.308	0.1	0.06616	0.03308	5.0	1.0	0.0
ETA0C	NC	ETAOT	NT	OVERC	OVERT	SRATE	REP0W
0.0	0.0	0.0	0.0	0.0	0.0	0.0	0.0

Table 4-Comparison of key results between test and FE model

Results Source	Critical Displacement (mm)		Critical Load (kN)		
	YL	PL	YL	PL	UL
Test	50	85.2	35	43.5	14.1
FEM	46.8	83.6	37.1	43.7	13.6
FEM/Test	0.936	0.981	1.06	1.005	0.965

Note: YL, PL, and UL represent yield load, peak load, and ultimate load, respectively.

1
2
3
4
5
6
7
8
9
10
11
12
13
14
15
16
17
18
19
20
21
22
23
24
471
25
26
472
27
28
29
473
30
31
32
33
34
35
36
37
38
39
40
41
42
43
44
45
46
47
48
49
50
51
474
52
53
475
54
55
56
476
57
58
59
60
61
62
63
64
65

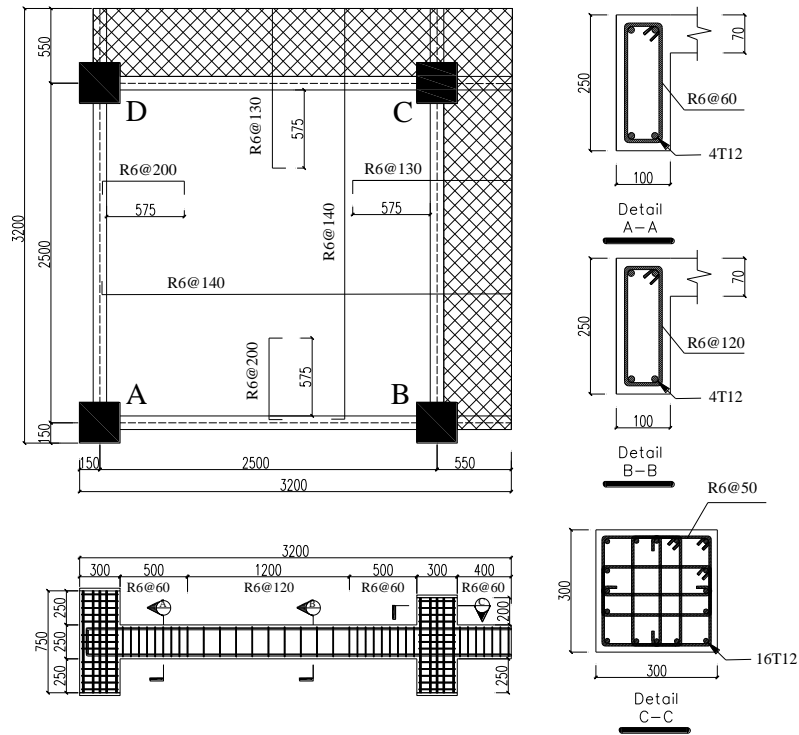


Fig. 1 Dimensions of Specimen US (units: mm) [5]

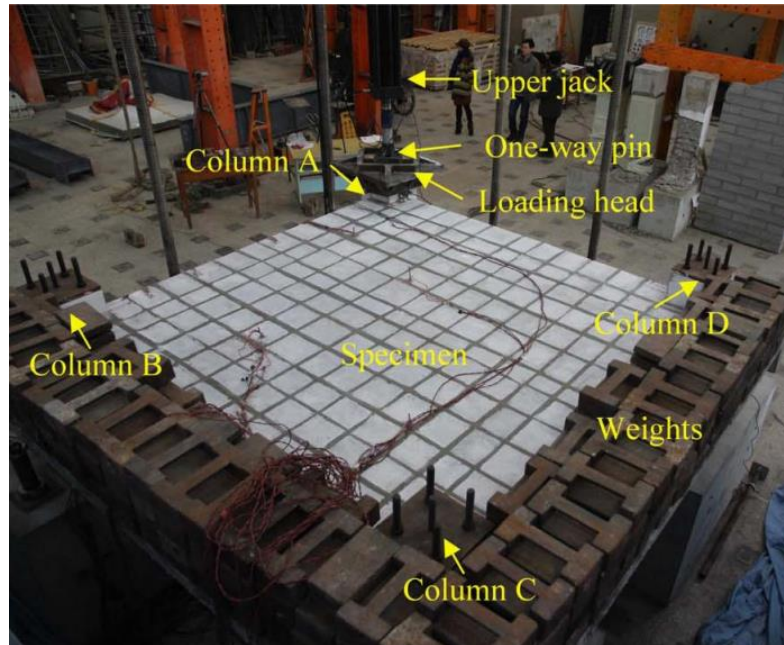


Fig. 2 Test setup and instrumentation location in the referenced experiment [5]

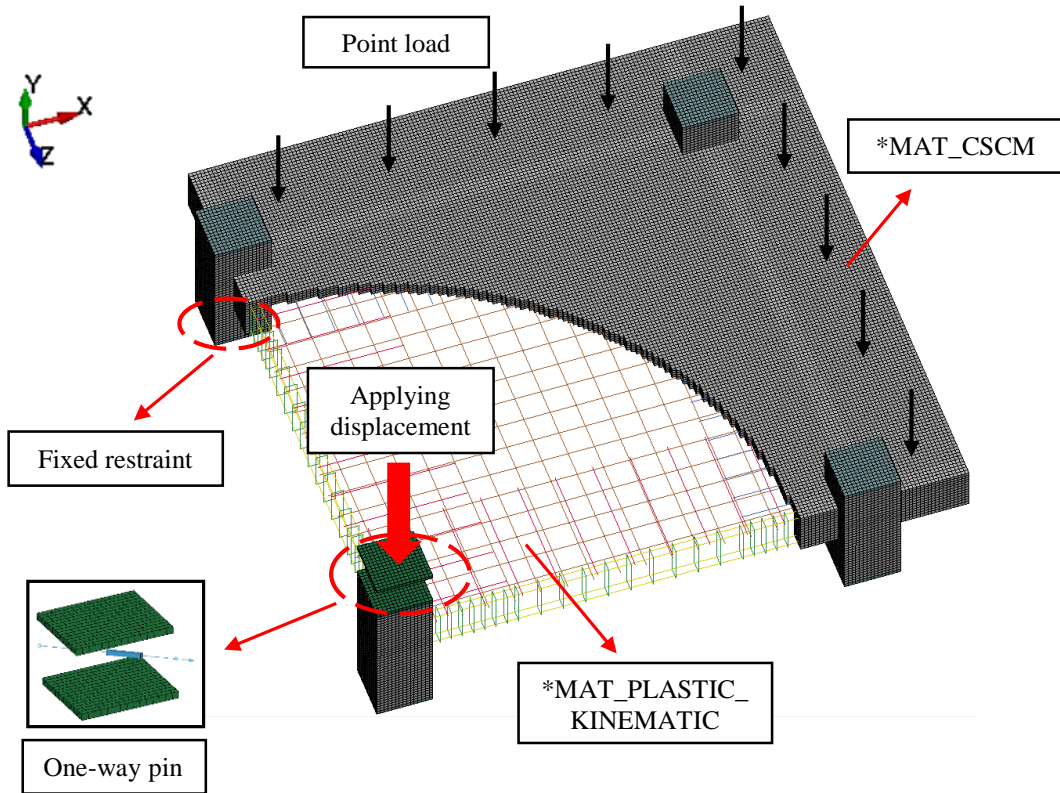


Fig. 3 Numerical model of US-CL-1F

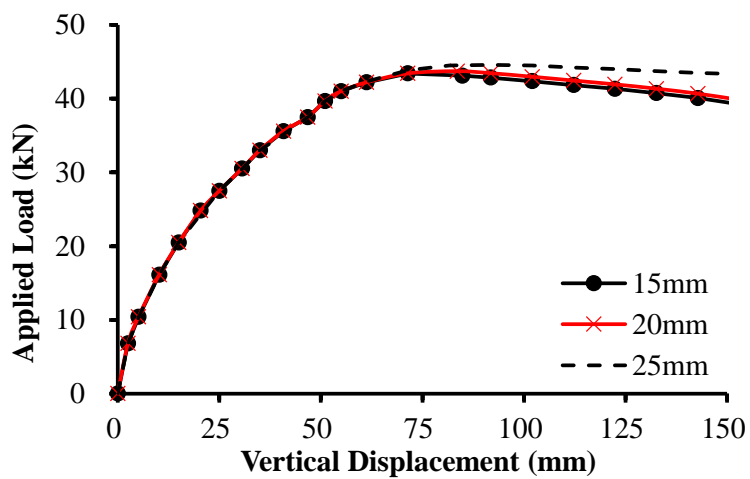


Fig. 4 Comparison of different mesh sizes

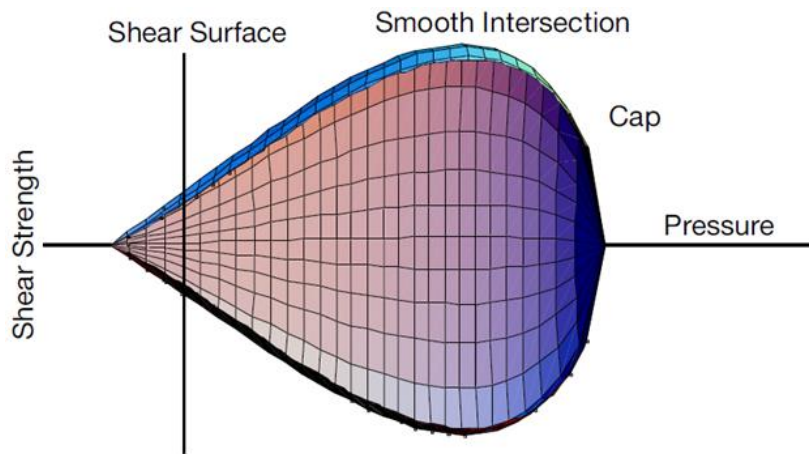


Fig. 5 General shape of concrete model yield surface

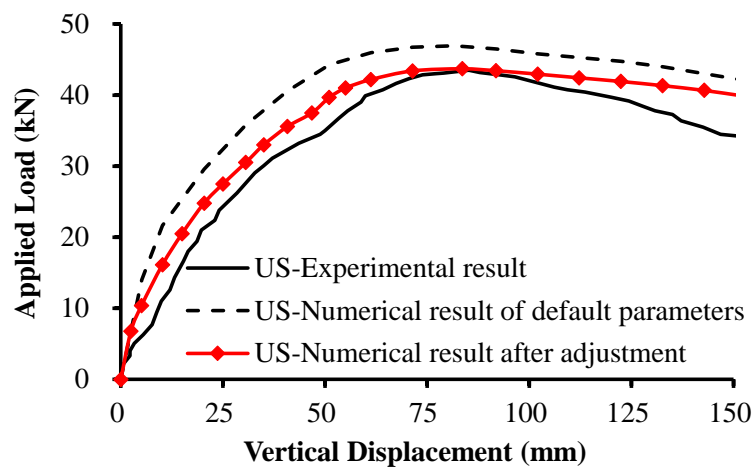


Fig. 6 Comparison of different concrete input parameters

1
2
3
4
5
6
7
8
9
10
11
12
13
14
15
16
17
18
19
20
21
22
23
24
25
26
27
28
29
30
31
32
33
34
35
36
37
38
39
40
41
42
43
44
45
46
47
48
49
50
51
52
53
54
55
56
57
58
59
60
61
62
63
64
65

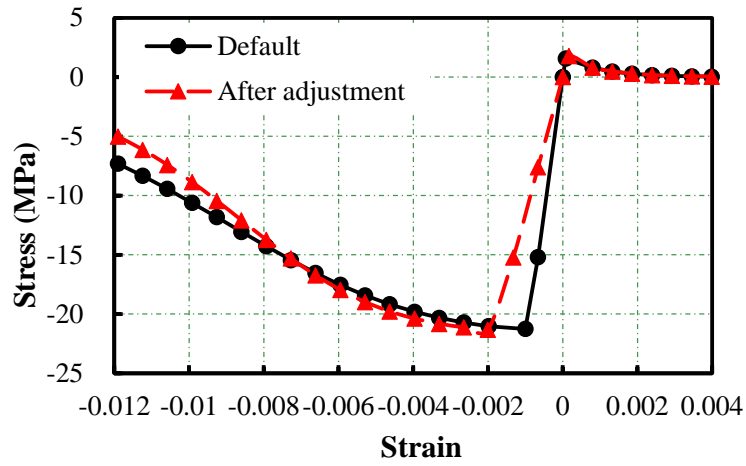


Fig. 7 Unconfined uniaxial stress-strain curve of concrete based on CSCM

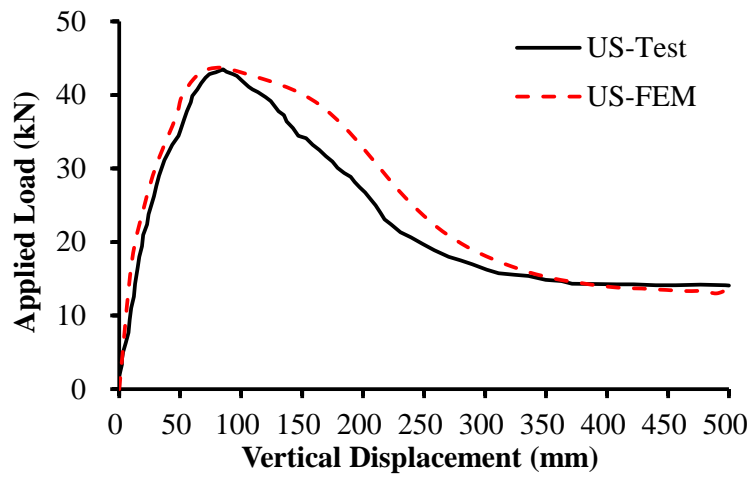
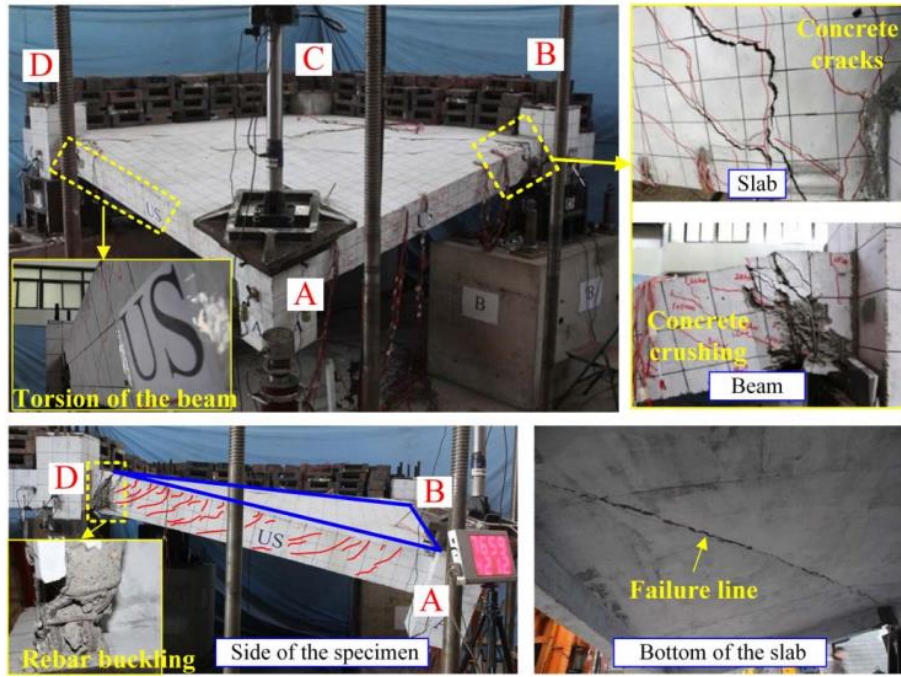
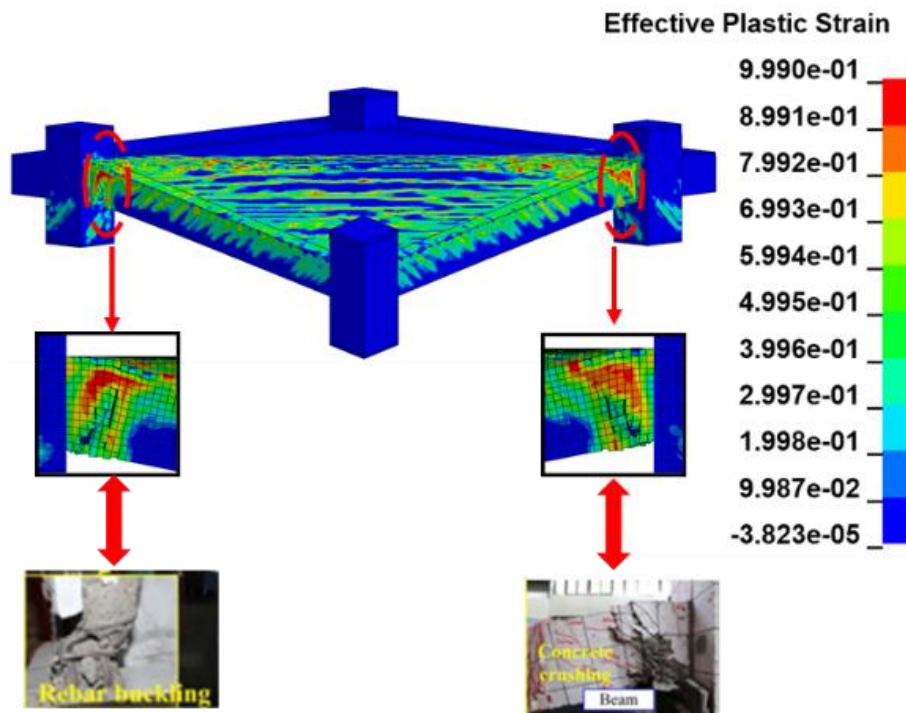


Fig. 8 Comparison of load-displacement curves between test and FE model



(a)

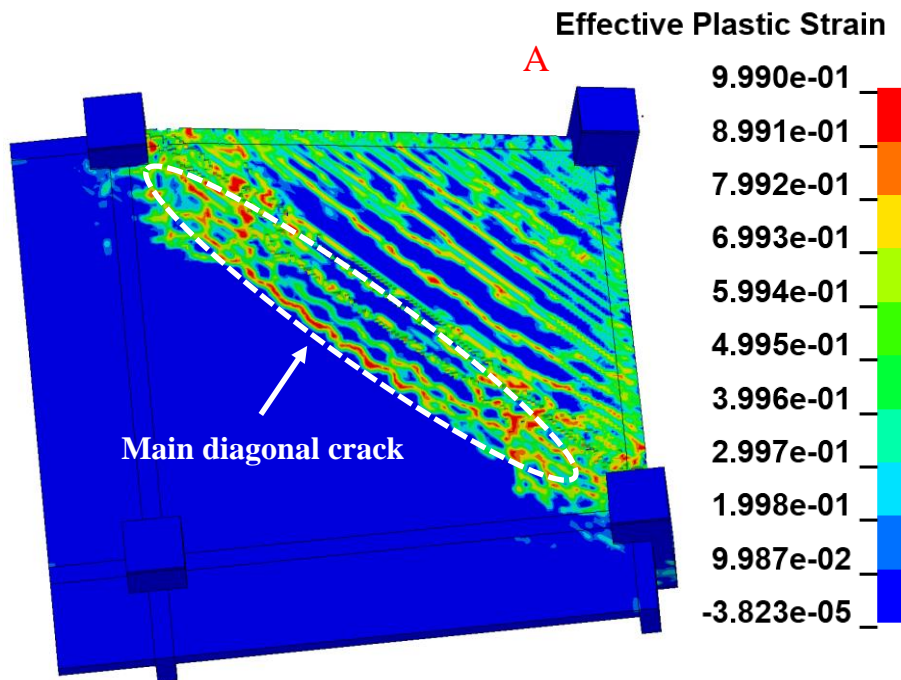


(b)

Fig. 9 Comparison of failure modes between test and FE model: (a) US [5]; (b) US-CL-1F



(a)



(b)

Fig. 10 Comparison of the crack distributions between test and FE model: (a) US [5]; (b) US-CL-1F

1
2
3
4
5
6
7
8
9
10
11
12
13
14
15
16
17
18
19
20
21
22
23
24
25
26
27
28
29
30
31
32
33
34
35
36
37
38
39
40
41
42
43
44
45
46
47
48
49
50
51
52
53
54
55
56
57
58
59
60
61
62
63
64
65

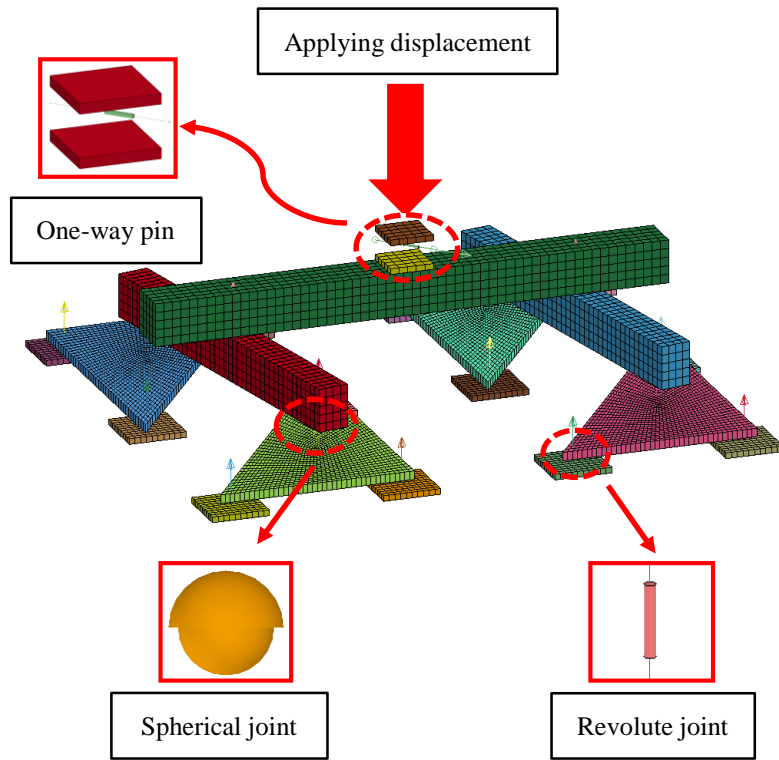


Fig. 11 Details of numerical model for load distribution rig

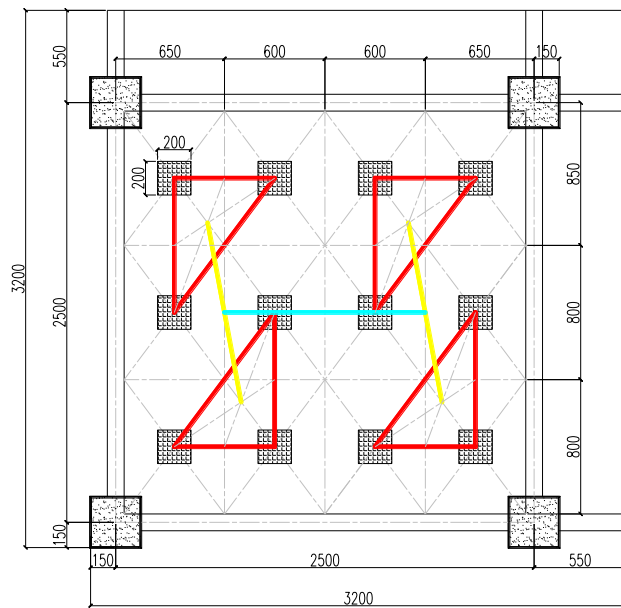


Fig. 12 Layout of the loading system (unit: mm)

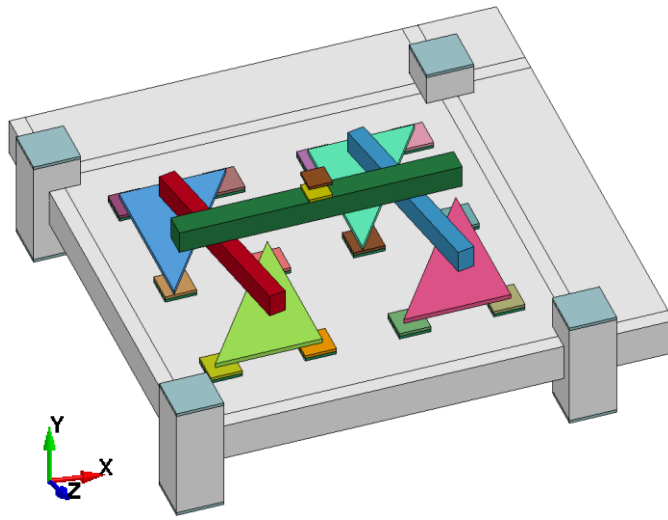


Fig. 13 Numerical model of US-UDL-1F

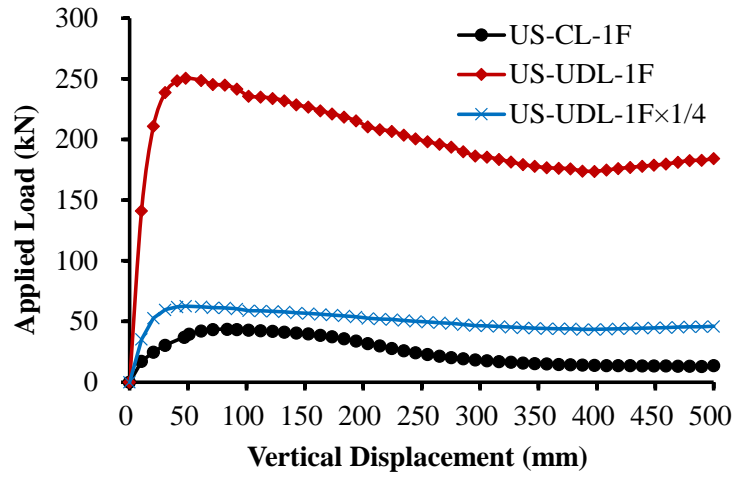
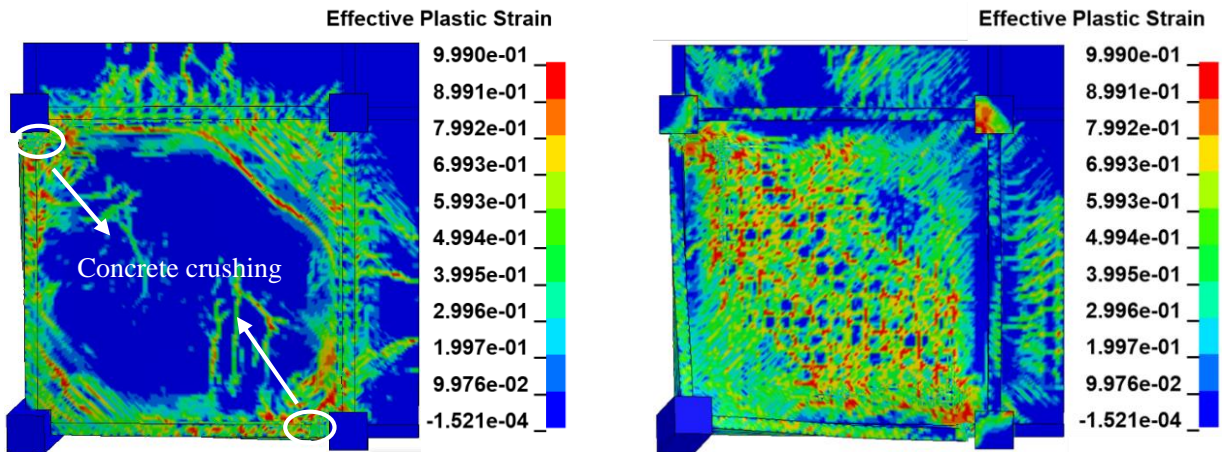


Fig. 14 Comparison of load-displacement curves between US-CL-1F and US-UDL-1F



525

(a)

(b)

1

526

Fig. 15 Failure modes of the slab in model US-UDL-1F: (a) Top surface of the slab; (b) Bottom

3

4

527

surface of the slab

6

528

9

10

11

12

13

14

15

16

17

18

19

20

21

22

23

24

25

529

26

27

28

29

30

31

32

33

34

35

36

37

38

39

40

41

42

43

44

45

46

47

48

49

50

533

Fig. 16 Development of beam axial force: (a) US-CL-1F; (b) US-UDL-1F

58

59

60

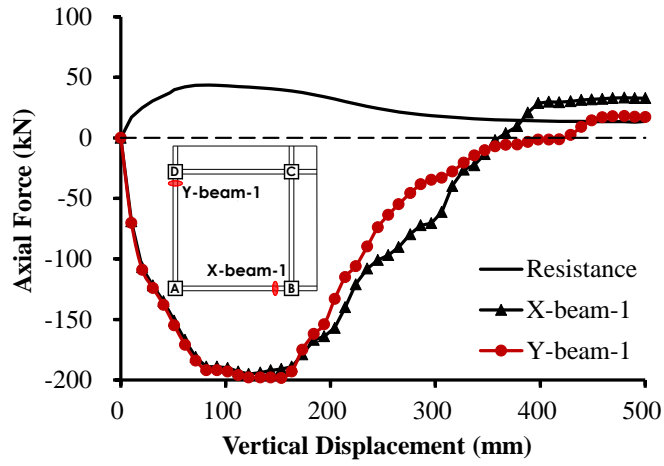
61

62

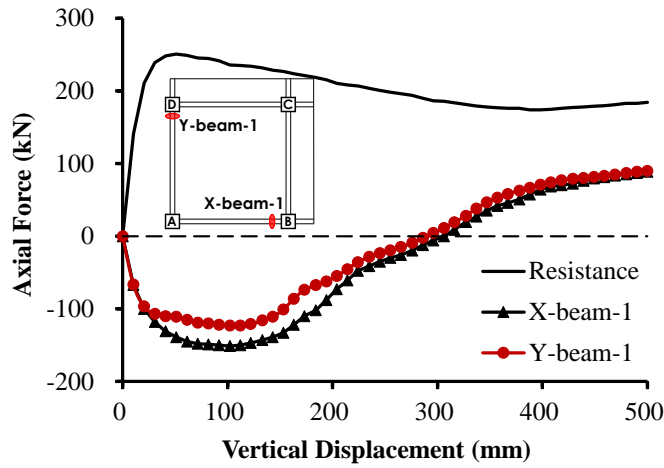
63

64

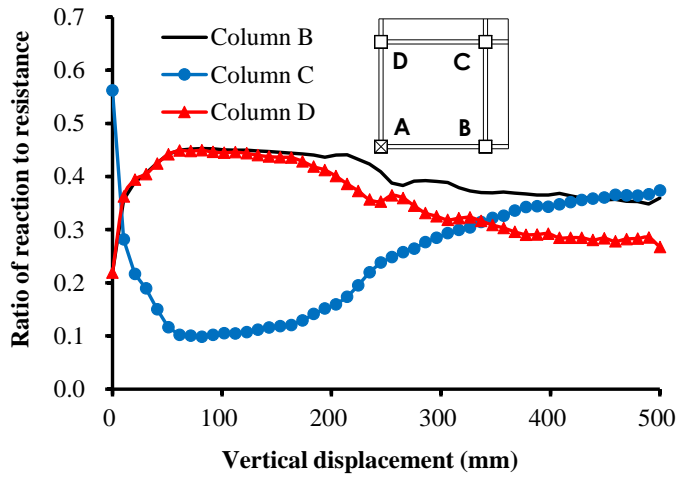
65



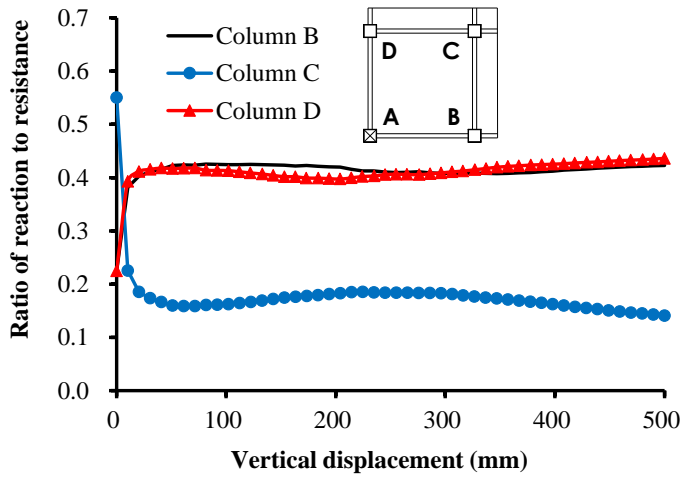
(a)



(b)



(a)



(b)

Fig. 17 Contribution of each supporting column: (a) US-CL-1F; (b) US-UDL-1F

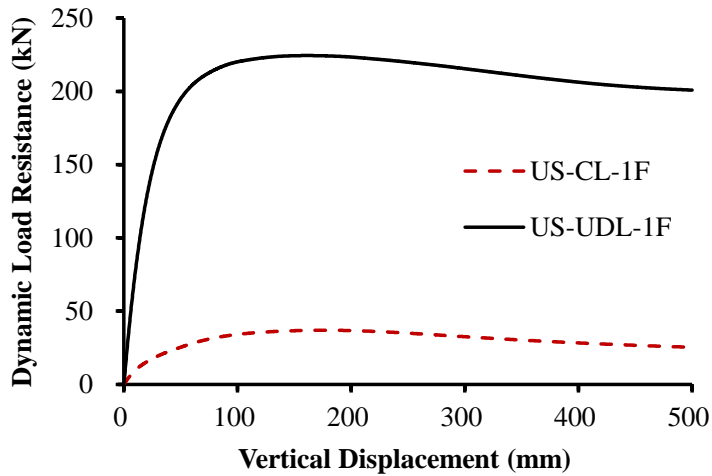


Fig. 18 Dynamic resistance of beam-slab substructures

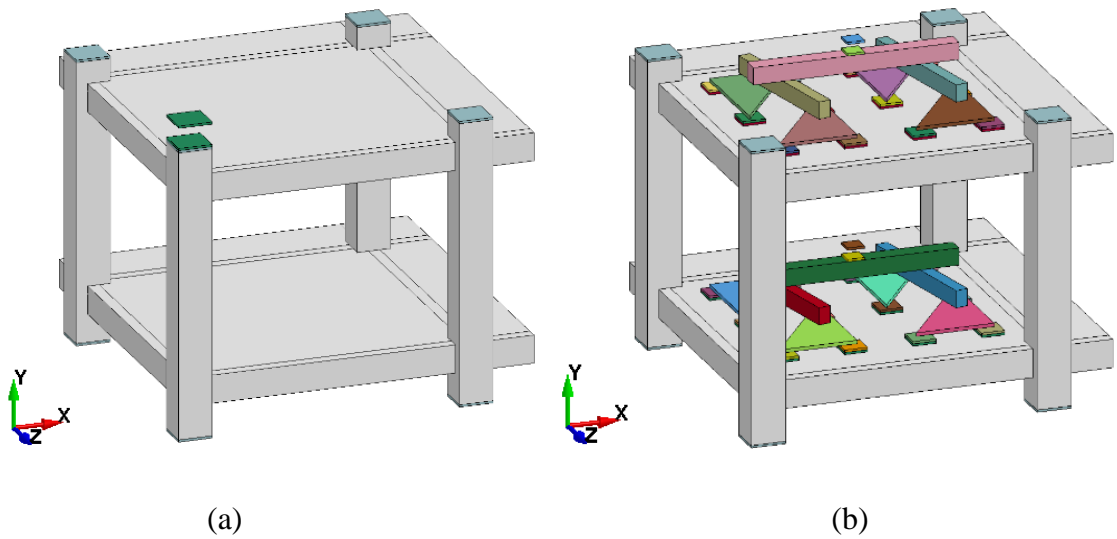


Fig. 19 Numerical models: (a) US-CL-2F; (b) US-UDL-2F

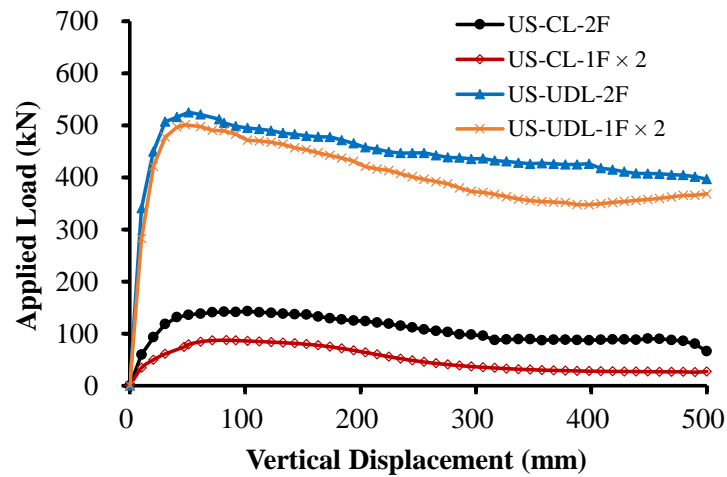


Fig. 20 Comparison of load-displacement curves between CL and UDL conditions

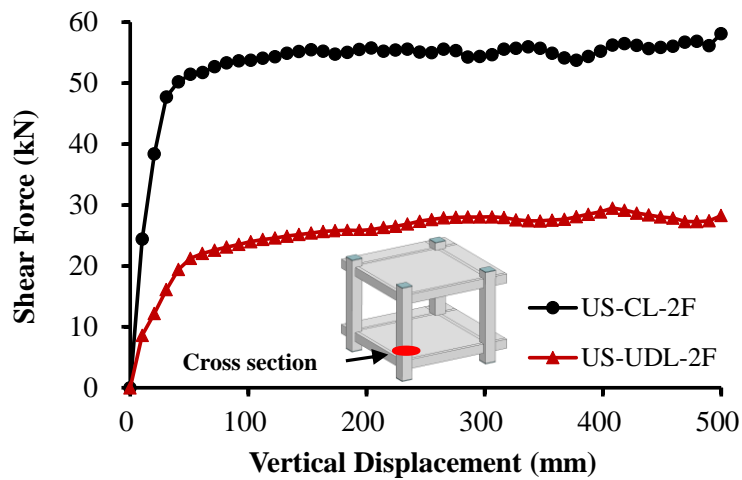
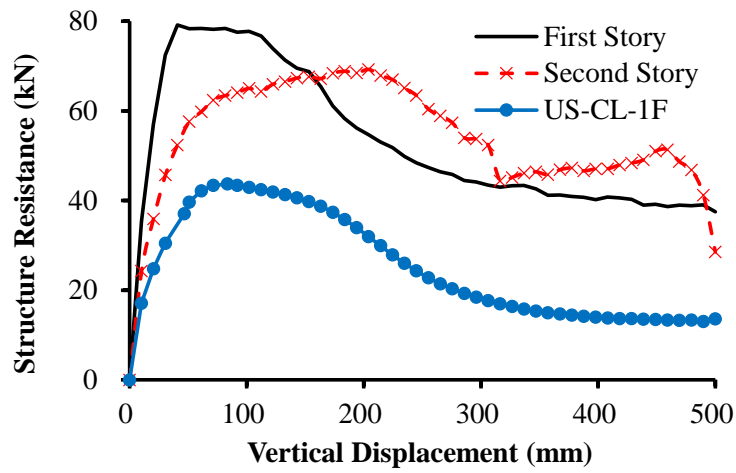
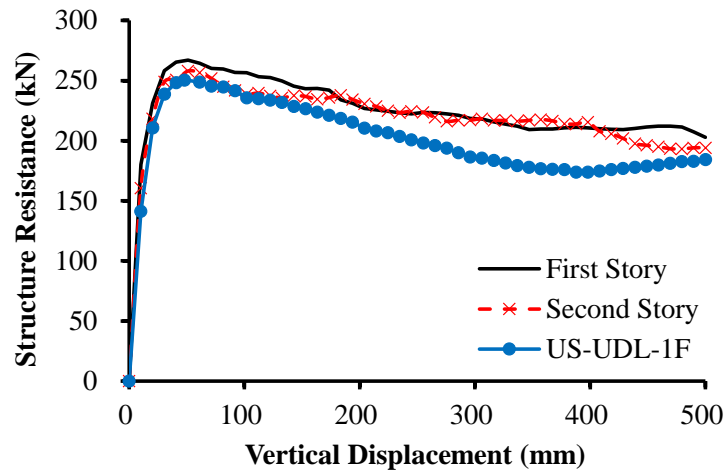


Fig. 21 Development of shear force of corner column



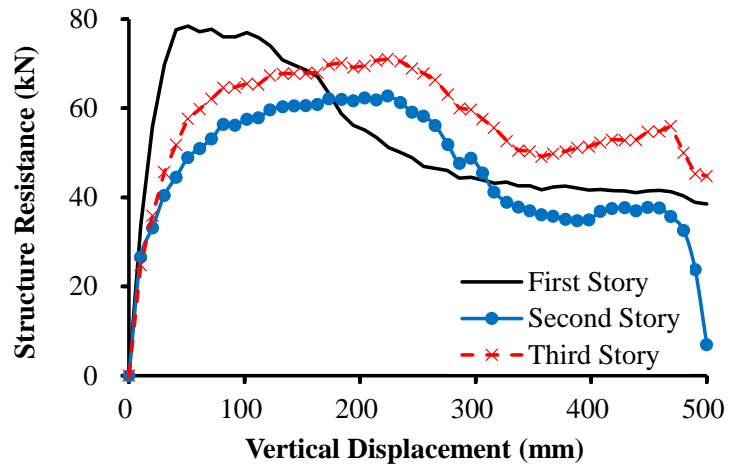
(a)



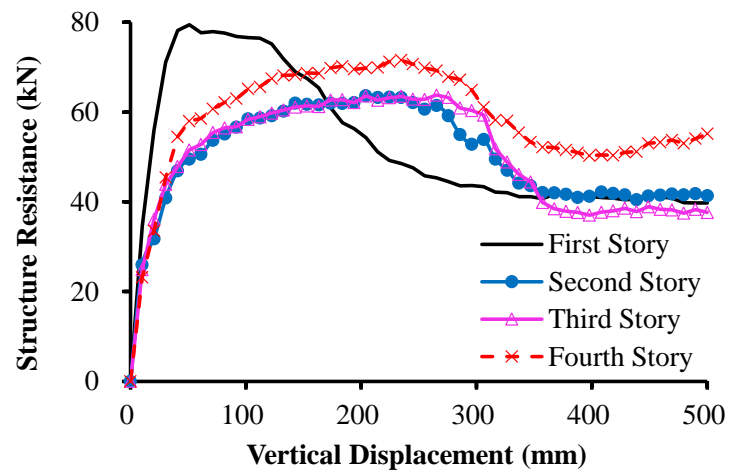
(b)

Fig. 22 Comparison of load resistance from different stories with single-story substructure:

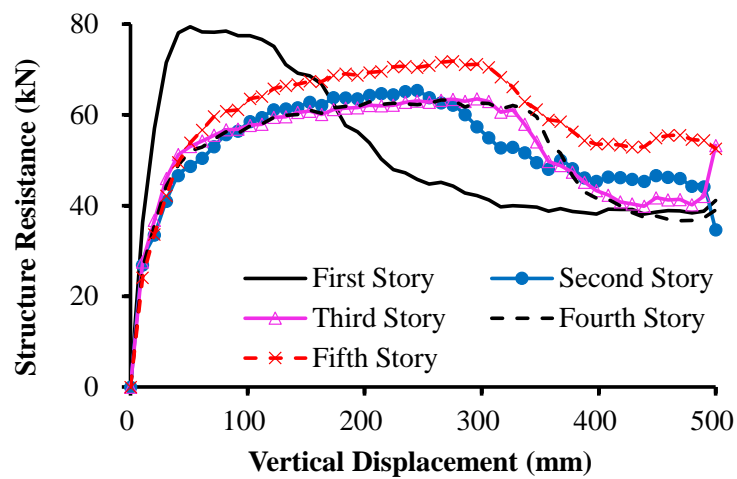
(a) US-CL-2F; (b) US-UDL-2F



(a)

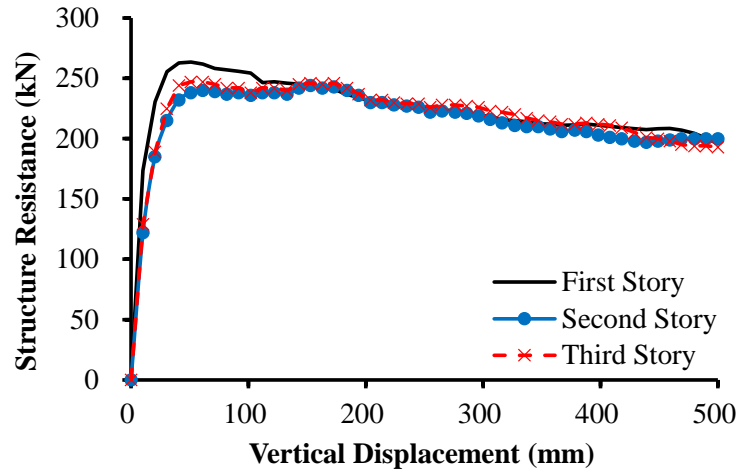


(b)

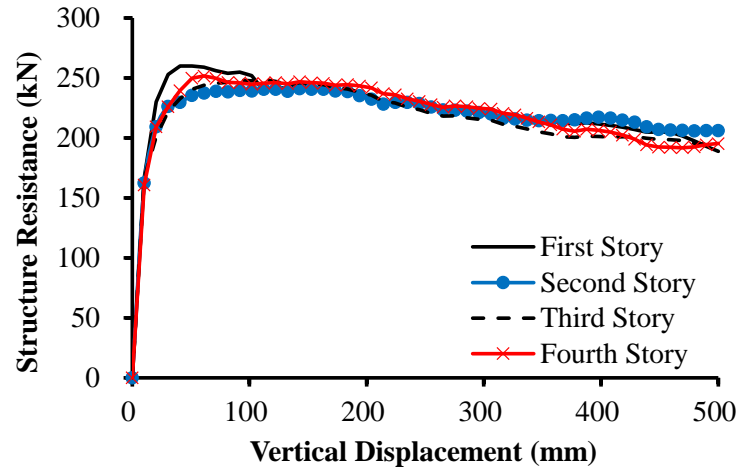


(c)

Fig. 23 Load resistance of each story under CL: (a) US-CL-3F; (b) US-CL-4F; (c) US-CL-5F

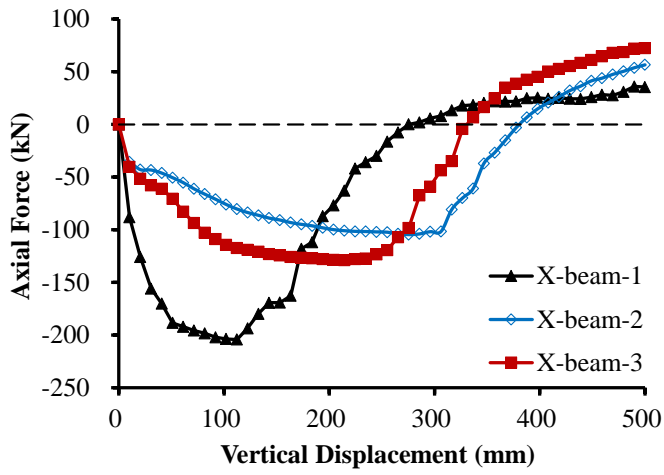


(a)

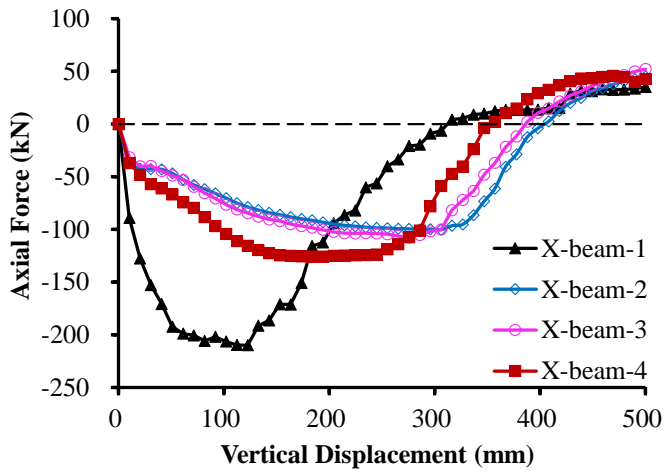


(b)

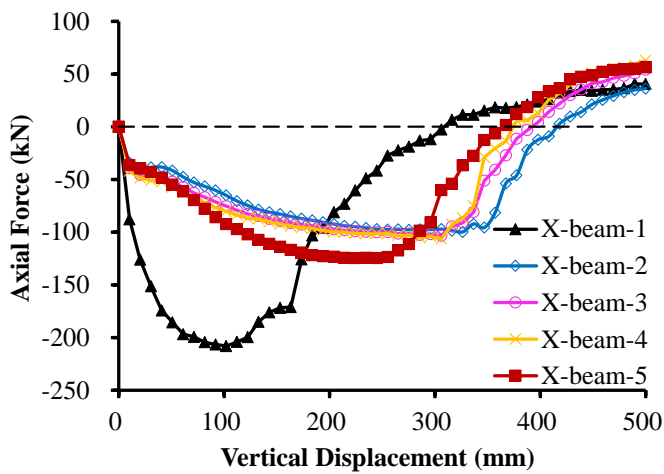
Fig. 24 Load resistance of each story under UDL: (a) US-UDL-3F; (b) US-UDL-4F



(a)

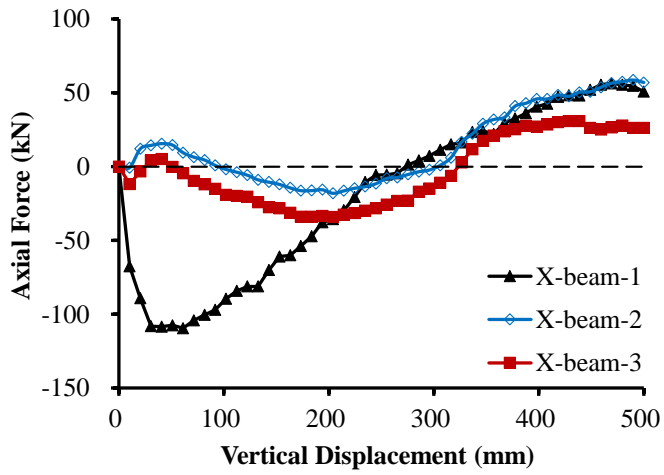


(b)

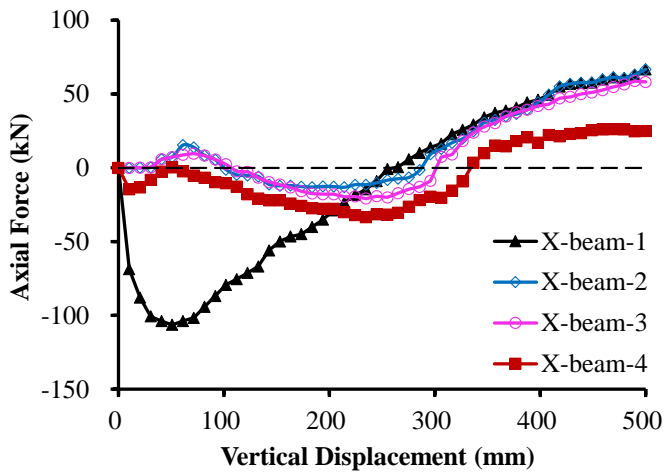


(c)

Fig. 25 Beam axial force of each story under CL: (a) US-CL-3F; (b) US-CL-4F; (c) US-CL-5F



(a)



(b)

Fig. 26 Beam axial force of each story under UDL: (a) US-UDL-3F; (b) US-UDL-4F

Dear Editor

This manuscript has no conflict of interest.

Please contact with the corresponding author (Kai Qian) by E-mail: qiankai@ntu.edu.cn, if necessary. Thank you so much!

Regards
Kai Qian

Author Statements

Kai Qian: Conceptualization. **Jian-Fei Cheng:** Methodology and Formal Analysis. **Yun-Hao Weng:** Writing- Original Draft Preparation. **Feng FU:** Writing- Original Draft Preparation.

Effect of Loading Methods on Progressive Collapse Behavior of RC Beam-Slab Substructures under Corner Column Removal Scenario

Kai Qian^{1,2*}, Jian-Fei Cheng¹, Yun-Hao Weng¹, Feng Fu³

¹College of Civil Engineering and Architecture, Guangxi University, Nanning, China, 530004.

²College of Civil Engineering and Architecture, Guilin University of Technology, Guilin, China, 541004.

³School of Mathematics, Computer Science and Engineering, City, University of London, U.K, EC1V 0HB.

Abstract: In this paper, high-fidelity finite element (FE) models were developed to investigate the behavior of reinforced concrete (RC) beam-slab substructures to resist progressive collapse under a corner column removal scenario. The numerical models were validated by test results. Then, the validated FE models were employed to investigate the structural behavior under different loading methods, including concentrated loading (CL) and uniformly distributed loading (UDL) methods. Moreover, multi-story frames were built to capture the load redistribution behavior of substructures at different floors under different loading methods. The results indicated that the loading methods affect overall structural responses, load transfer mechanisms, and failure modes. It was demonstrated that the Vierendeel action could not be ignored for multi-story frames to resist progressive collapse caused by the loss of a corner column scenario. More significant Vierendeel action was developed in the structure subjected to CL method than that subjected to UDL method. It was also found that the load transfer mechanisms developed in the top story and bottom story for a multi-story frame are pretty different from those in the middle stories. The bottom story has the most remarkable load resisting capacity.

Keywords: Progressive collapse; Loading method; Load transfer mechanism; Corner column removal.

* Corresponding author. E-mail address: qiankai@glut.edu.cn

23 1. Introduction

24 ASCE/SEI-10 (2010) [1] defines progressive collapse as the spread of an initial local failure from
25 element to element, eventually resulting in the collapse of the entire structure or a large part of it
26 disproportionately. Progressive collapse first attracted public attention after the partial collapse of Ronan
27 Point apartment in London. The research topic became popular after the collapse of Alfred P. Murrah
28 Federal Building in Oklahoma City and World Trade Center in New York. To date, several codes and
29 design guidelines (ASCE/SEI-10 2010 [1]; General Services Administration (GSA) 2003 [2];
30 Department of Defense (DoD) 2009 [3]) had been issued for practical engineers to design buildings in
31 mitigating progressive collapse. There are two main methods commonly suggested by design guidelines:
32 direct and indirect design methods. Due to the uncertainty of extreme events, the alternate load path
33 (ALP) method, one of the direct design methods, has been considered as a major technique as it is event-
34 independent.

35 In the past decades, numerous experimental studies [4-18] and numerical simulations [19-25] have
36 been conducted to investigate the progressive collapse behavior of reinforced concrete (RC) and precast
37 concrete (PC) structures based on the ALP method. Remarkable efforts have been made towards deeper
38 understanding of load transfer mechanisms, such as compressive arch action (CAA) [4-6], tensile
39 catenary action (TCA) [7-9] developed in beams, and compressive membrane action (CMA) [11,12],
40 tensile membrane action (TMA) in slabs [20,21]. Zhou et al. [4] conducted a series of static tests on a
41 one-third scaled RC specimen and two PC specimens using dowel bars and corbel to investigate the load
42 transfer mechanisms of these specimens under a middle column loss. Feng et al. [5] investigated the
43 progressive collapse behavior of four beam-slab substructures subjected to a corner column loss. It was

44 found that the development of TCA was limited due to weak horizontal constraints from the surrounding
45 elements. Sasani [6] investigated the dynamic response of a 6-story RC frame subjected to simultaneous
46 removal of a corner column and an adjacent exterior column. They concluded that the three-dimensional
47 Vierendeel action plays a key role **in** load redistribution. It should be noted that the maximum vertical
48 displacement was so low that no CAA and TCA were developed. Lu et al. [9] and Ren et al. [10]
49 conducted several series of laboratory tests on RC specimens with or without slabs. In their tests, both
50 the middle and edge column removal scenarios were investigated. It was found that the effects of beam
51 height, slab thickness, and seismic reinforcing details **dominate** the progressive collapse resistance of
52 RC frames.

53 It should be noted that the majority of existing tests relied on the concentrated loading (CL) method,
54 which applied a concentrated load on the removed column. However, in reality, the load was uniformly
55 distributed on the slab or beam. **Thus, the uniformly distributed loading (UDL) method should be applied**
56 **to represent real load patterns. However, for UDL method, the weights were increased slowly to simulate**
57 **the increment of UDL, which should be very dangerous when reached the ultimate load capacity. In**
58 **addition, the softening branch of the load-displacement curve could not be captured. To overcome this**
59 **drawback, as an alternative method, the multi-points loading method (equivalent UDL), which was a**
60 **displacement-controlled method, was widely adopted in previous investigations [15-19,21]. Qian et al.**
61 **[15] carried out a series of RC beam-slab substructures under different column missing scenarios. The**
62 **UDL method was equivalently applied on the slab by a specially designed loading frame. Pham et al.**
63 **[17] also adopted the loading tree to equivalently apply UDL on progressive collapse performance of**
64 **beam-slab substructures under the loss of an exterior column scenario. Moreover, flat slab or flat plate**

65 substructures were tested under the equivalent UDL method to investigate the effects of loading methods
66 subjected to an interior column removal scenario [16,19].

67 The effects of loading methods on performance of RC substructures have been explored [18, 21].
68 The influence of loading methods on the behavior of buildings subjected to the loss of a corner column
69 is still unclear due to insufficient investigations. Moreover, previous investigation was focused on single-
70 story substructures [5,13], which has to ignore the Vierendeel action, one of the important load resisting
71 mechanisms for RC frames subjected to the loss of a corner column scenario. Thus, in this study, high
72 fidelity finite element (FE) models were developed to quantify the effects of different loading methods
73 on the performance of RC frames to resist progressive collapse caused by the loss of a corner column
74 scenario. Furthermore, multi-story frames were built to investigate the efficiency of Vierendeel action
75 and quantify the mobilization of load transfer mechanisms among different stories with various loading
76 methods.

77 **2. Experimental program and numerical validation**

78 **2.1. Brief of the experimental program**

79 Before conducting this numerical study, the FE model was validated by the experimental results of
80 Feng et al. [5]. The experimental program [5] will be introduced briefly for readers easy to understand
81 the validation and FE models. A seismically designed 6-story RC prototype building was designed
82 following Chinese codes [26,27], with a height of 3900 mm in the first story and 3600 mm in upper
83 stories. The span length in both directions was 5000 mm. The dead load (DL) and live load (LL) were
84 5.5 and 2.0 kPa, respectively. Four 1/2 scaled RC beam-slab substructures were tested subjected to the
85 loss of a corner column scenario. However, only the results of Specimen US from Feng et al. [5] were

86 used for validation in this study. The dimensions and reinforcement details of Specimen US are shown
87 in Fig. 1. The overall dimension was 3200 mm × 3200 mm. The cross-section of the beam and column
88 was 100 mm × 250 mm and 300 mm × 300 mm, respectively. The slab thickness was 70 mm. The
89 transverse reinforcement was bent up 135° and was also installed in the beam-column joints in
90 accordance with seismic RC detailing. The typical experimental setup and instrumentations are shown
91 in Fig. 2. Three column supports were fixed to the RC blocks, which were fixed to the strong floor by
92 bolts. To simulate the additional constraints from the surrounding slabs, a uniformly distributed load of
93 12.0 kN/m² was applied on the extending part of the slab. The load combination of (2DL+0.5LL) is
94 selected, as suggested by GSA 2003 [2]. It should be noted that a one-way pin was installed between the
95 hydraulic jack and the top of the corner column stub to allow the corner column stub to rotate and to
96 ensure no extra bending will be introduced in the loading process. Thus, Vierendeel action of the frames
97 can be neglected in this experimental program. A displacement-controlled CL manner was adopted.

98 The average cubic compressive strength of the concrete of Specimen US was 26.6 MPa, which
99 corresponded to the cylinder compressive strength of 21.3 MPa. The measured reinforcement properties
100 are tabulated in Table 1. For detail of test results, please refer to Feng et al. [5].

101 2.2. Numerical model setup

102 Commercial software LS-DYNA was adopted in this numerical study. Explicit solver was adopted
103 to avoid divergence problems. The geometric model of Specimen US is shown in Fig. 3. Similar
104 geometric dimensions, reinforcement details, and boundary conditions to the experimental test [5] were
105 used in this numerical model.

106 2.2.1. *Element types*

107 As shown in Fig. 3, both concrete and steel plates were simulated by 8-node solid elements with a
108 reducing integration scheme. There was one integration point in each solid element, which can
109 considerably save computational time on the premise of accuracy when hourglass control is
110 appropriately defined. To ensure the hourglass energy was less than 10% of the total internal energy, the
111 hourglass coefficient was determined as 0.001. Flanagan-Belytschko stiffness form with exact volume
112 integration was used. Moreover, reinforcements were modeled using 2-node Hughes-Liu beam elements
113 with 2×2 Gauss quadrature integration. This beam formulation could effectively simulate the mechanical
114 property of reinforcements, such as axial force, bi-axial bending, and transverse shear strain.

115 In this study, sensitivity analysis with three different mesh sizes of 25 mm, 20 mm, and 15 mm are
116 conducted, as tabulated in Table 2. As shown in Fig. 4, mesh size of 20 mm is adequate, as further mesh
117 refinement will not further enhance the accuracy significantly. As a result, the mesh size of concrete
118 element is chosen as $20 \text{ mm} \times 20 \text{ mm} \times 17.5 \text{ mm}$ for RC slabs and $20 \text{ mm} \times 20 \text{ mm} \times 20 \text{ mm}$ for other
119 components. The size of beam element is 20 mm.

120 2.2.2. *Material model*

121 Several constitutive models are available in the material library of LS-DYNA. In this study,
122 continuous surface cap model (CSCM) is used for concrete as it could effectively simulate the
123 mechanical property of concrete, including damage-based softening, modulus reduction, shear dilation,
124 shear compaction, confinement effect, and strain rate effect [28]. The failure of CSCM model is
125 controlled by the shear failure surface and hardening cap surface [29], as shown in Fig. 5. And the yield
126 surface is formed based on three stress invariants J_1 , J_2 , and J_3 . Previous studies [19-23] found that
127 erosion criterion based on the maximum principal strain is a suitable way to simulate concrete crushing

128 or spalling under both quasi-static and dynamic conditions. However, it could not simulate shear failure
129 well when only the maximum principal strain was adopted for the definition of erosion criterion. Thus,
130 Weng et al. [19] suggested that the maximum principal strain and shear strain criteria should be
131 considered simultaneously by using keyword *Mat_Add_Erosion. Since the appropriate values are
132 dependent on the mesh size, the value of maximum principal strain and shear strain is set to 0.08 and 0.3
133 based on multiple trials. Once the maximum principal strain or shear strain is reached, the solid element
134 is deleted. Furthermore, the strain rate effect was ignored since only quasi-static behavior was discussed
135 in this study.

136 LS-DYNA provides a simplified way to define CSCM (*Mat_CSCM_CONCRETE) for concrete
137 properties, which only needs three input parameters (unconfined compressive strength f'_c , maximum
138 aggregate size A_g , and units). Then the remaining material properties are calculated automatically
139 according to equations proposed by CEB-FIP concrete model code [30]. But the simplified CSCM is
140 suited for f'_c between 28 MPa and 58 MPa. Since the unconfined compressive strength f'_c of
141 Specimens US was 21.3 MPa, the original CSCM (*Mat_CSCM) is used, which requires a series of
142 input parameters to define concrete material properties, as shown in Table 3.

143 However, the default concrete material properties would overestimate the initial stiffness and
144 structural resistance, as shown in Fig. 6. Therefore, a few adjustments on the elasticity modulus and
145 fracture energy of concrete were made to improve the numerical results. Previous studies [19-21,23]
146 suggested that the tensile fracture energy G_{ft} could be reduced to 80% of the default one when it is over
147 predicted. If shear or compressive-based damage is significant, the shear fracture energy G_{fs} should be
148 set as $G_{fs} = 0.5G_{ft}$ and $G_{fc} = 50G_{ft}$. However, the default is $G_{fs} = 100G_{ft}$. In this study, since severe flexural
149 and torsional failure occurred in the beam ends in Specimen US, both G_{ft} and G_{fs} were adjusted herein.

150 The detailed parameters of CSCM are listed in Table 3. The unconfined uniaxial stress-strain relationship
151 of concrete after adjustments is shown in Fig. 7. The initial stiffness is lower than that of the default one,
152 and the compressive stress reduces faster in the softening stage. As shown in Fig. 6, the adjusted material
153 property could improve the numerical results significantly.

154 The symmetric bilinear elastic-plastic material model (*Mat_Plastic_Kinematic) is used for
155 reinforcements, which assumes the tensile behavior is identical to that of compressive. The parameters
156 of material properties, including elastic modulus, yield strength, tangential modulus, and ultimate strain,
157 are determined based on the material tests. When the strain exceeds the ultimate elongation ratio, the
158 corresponding reinforcement element is also deleted. The strain rate effect was ignored since only quasi-
159 static behavior was discussed in this study. As suggested by previous works [19,23], a perfect bonding
160 between concrete and reinforcement was assumed based on *Constrained_Lagrange_In_Solid.

161 **2.2.3. Boundary conditions**

162 In the numerical modeling, similar to the experimental program, the uniformly distributed load was
163 applied on the extending area of the specimen. For simplicity, three concrete blocks were modeled using
164 three rigid plates with zero translations and rotations, as indicated in Fig. 3. Furthermore, a rigid plate
165 was generated at the top of the column stub to prevent stress concentration when concentrated loads
166 were applied. Single surface (*Contact_Automatic_Single_Surface) was defined between the rigid plate
167 and RC column. Besides, static and dynamic coefficients of friction were set as 1.0 at the contact surface
168 to prevent any sliding of the rigid plate. Similar to experimental work, a one-way pin was generated
169 between the loading plate and corner column by using constraint type *Constrained_Joint_Revolute.

170 **2.3. Validation of the numerical model**

171 Fig. 8 shows the comparison of load-displacement curves between the test results and FE model.
172 At a large deformation, the TCA in beams and tensile membrane action in slabs is not efficiently
173 mobilized due to the weak tie force from the surrounding structural members. Thus, the source of load
174 resistance is mainly attributed to flexural action or beam action. As shown in Fig. 8, the load-
175 displacement curve from FE model is quite similar to test results, including initial stiffness, yield load,
176 ultimate load, and ultimate deformation capacity. The error of key results between the FE model and test
177 one is less than 7 %, as listed in Table 4.

178 It is noted that the crack pattern of the RC beam-slab substructure cannot be directly demonstrated
179 because concrete model CSCM is unable to track cracks. However, the cracks can be equivalently
180 demonstrated by effective plastic strains. Generally, wider cracks expressed more significant effective
181 plastic strains. The concrete damage was quantified through the damage index. Damage index of 0 and
182 1 represents no damage and complete failure, respectively. As shown in Figs. 9 and 10, FE model could
183 effectively simulate concrete crushing or spalling of the beam and crack patterns of the slab.

184 As a result, the agreement of the load-displacement curves and the failure modes between the
185 numerical and test results indicated the validity of the numerical model. Thus, the model was used to
186 investigate the load transfer mechanisms of the RC frames with different loading methods and story
187 numbers.

188 **3. Effect of loading methods**

189 Due to the limitation of cost and test conditions, only an experimental study under CL condition
190 was conducted by Feng et al. [5]. However, UDL should be applied as gravity load and live load are

191 uniformly distributed along the structure. Thus, it is necessary to study the difference between these two
192 loading approaches. As a result, the validated FE model was utilized to evaluate the behavior of RC
193 beam-slab substructures under both CL and UDL methods.

194 **3.1. Details of UDL model**

195 Previous studies [15-19,21] had proved the effectiveness of the 12-point loading tree to simulate
196 the UDL scheme equivalently. Moreover, Weng et al. [19] modeled the load distribution rig with high
197 fidelity, and the reliability of the numerical model was proved. Thus, in this study, the same modeling
198 method was adopted to simulate the behavior of substructures under the UDL method. As shown in Fig.
199 11, the load distribution rig [19] consisted of a series of rigid beams and plates simulated by 8-node solid
200 elements. The connection between the top and the secondary rigid beam was defined by keyword
201 *Constrained_Joint_Revolute [19,21]. The connection between the secondary rigid beam and the
202 triangle rigid plate was also modeled by keyword *Constrained_Joint_Revolute. The bottom steel plate
203 was connected with the triangle steel plate by revolute joints to ensure the bottom plates could rotate. In
204 addition, a contact function was used between the load distribution rig and RC frame by
205 *Contact_Automatic_Single_Surface [19]. A one-way pin was also defined between the loading plate
206 and the top rigid beam so that the top rigid beam was able to rotate around the one-way pin. In this study,
207 each loading point coincided with the centroids of 12 sub-areas, as indicated in Fig. 12.

208 As shown in Fig. 13, a beam-slab substructure under the UDL method named US-UDL-1F was
209 built based on the validated model of US-CL-1F. It should be noted that the dimensions, reinforcement
210 details, and boundary conditions of US-UDL-1F are identical to those of US-CL-1F.

211 **3.2. Structural resistance**

212 Fig. 14 shows the comparison of the load-displacement curves from different loading schemes. As
213 shown in the figure, the peak load of 43.7 kN and 250.6 kN was measured at US-CL-1F and US-UDL-
214 1F, respectively. The initial stiffness, which is defined as the ratio of peak load to the corresponding
215 displacement, of US-CL-1F and US-UDL-1F is 0.52 kN/mm and 5.2 kN/mm, respectively. Thus, the
216 UDL method increases the peak load and initial stiffness by 473% and 897%, respectively. However, it
217 should be noted that the load capacity from US-UDL-1F should be divided by four before comparing it
218 with US-CL-1F based on a simple load distribution analysis. Thus, as shown in Fig. 14, the load-
219 displacement curve of one-quarter of US-UDL-1F is generally more significant than that of US-CL-1F
220 as the slab deformation of US-UDL-1F is more uniform. No major diagonal crack is formed, and more
221 negative yield lines are observed at the top slab, as shown in Fig. 15.

222 **3.3. Load redistribution of beam-slab substructures**

223 To reveal the difference in load transfer mechanisms of the RC beam-slab substructures with
224 different loading methods, the results of the internal forces of beams and columns were extracted. It
225 should be noted that the beam sections are at a distance of 200 mm away from the beam-column interface
226 to avoid element erosion and fail to provide the internal forces.

227 **3.3.1. Development of axial force in beams**

228 Fig. 16 shows the development of axial force at the cross-sections near the column stub. Due to
229 symmetry, similar characteristics of axial force development are observed at cross-sections X-beam-1
230 and Y-beam-1. The axial force initially is compressive, indicating the mobilization of CAA. For CL and

231 UDL methods, when the displacement exceeds 370 mm and 296 mm, respectively, the axial force
232 transfers into tension, reflecting the development of TCA.

233 The comparison between Fig. 16 (a) and (b) indicates that the UDL method significantly weakens
234 the CAA of beams (e.g., the maximum axial compressive force reduces from 198.3 kN to 151.2 kN) but
235 starts the TCA earlier and greater. For CL and UDL methods, the maximum axial tension force is 38.1
236 kN and 98.1 kN, respectively, which indicates that TCA is not efficiently mobilized due to fewer
237 constraints from surrounding structural members.

238 3.3.2. Reactions of supporting columns

239 Figs. 17 (a) and (b) demonstrate the proportion of reaction force at different columns to the total
240 reaction force under CL and UDL, respectively. For US-CL-1F, at the displacement of 50 mm, 44% and
241 44% of the load is distributed into columns B and D, respectively. Similarly, at this displacement stage,
242 42% and 42% of the load are distributed into columns B and D of US-UDL-1F. For US-CL-1F, after
243 displacement of 82 mm, the proportion of columns B and D decreases with further increasing the
244 displacement due to concrete crushing occurred at the beam AB and AD. Conversely, the proportion of
245 column C keeps growing as column C remains almost intact during the test. However, for US-UDL-1F,
246 after displacement of 20 mm, the proportion of columns B, C, and D nearly maintains constant because
247 the deformation of the slab and beam is more uniform. In other words, column C suffers more significant
248 damage when increasing the displacement.

249 3.4. Dynamic response

250 It is worth noting that progressive collapse is normally a dynamic event. Thus, it is necessary to
251 evaluate the dynamic load capacity of the substructures under different loading methods. Based on

252 previous studies [8,14,15,22], an energy-based model, which was proposed by Izzuddin et al. [31], was
253 adopted in this dynamic evaluation. The dynamic resistance of the specimens could be determined by
254 Eq. (1).

$$255 \quad P_d(u_d) = \frac{1}{u_d} \int_0^{u_d} P_{NS}(u) du \quad (1)$$

256 where $P_d(u)$ and $P_{NS}(u)$ represent the dynamic load resisting function and nonlinear static load
257 resisting function, respectively.

258 Fig. 18 illustrates the dynamic behavior of the beam-slab substructures. The dynamic peak loads of
259 US-CL-1F and US-UDL-1F are 36.9 and 224.4 kN, respectively. Similar to the conclusions from
260 nonlinear quasi-static results, the UDL method could increase the dynamic peak load by 508%. Even,
261 the load resistance of US-UDL-1F is divided by four, the UDL method could increase the dynamic load
262 capacity of CL-case by 52 %.

263 4. Analysis of multi-story frame structures

264 Progressive collapse is a global behavior for a multi-story building. However, only a single-story
265 beam-slab substructure was tested in the test program [5]. Thus, it is imperative to understand whether
266 the load transfer mechanisms in the single-story substructure are the same as those in a multi-story
267 building. As shown in Fig. 19, US-CL-2F and US-UDL-2F were established, which represent a two-
268 story frame substructure under CL and UDL methods, respectively. It should be noted that the load
269 distribution tree, similar to US-UDL-1F, was generated in each story of US-UDL-2F.

270 4.1. The role of Vierendeel action

271 As concluded by Sasani [6], in moment frames, Vierendeel action is the major mechanism for the
272 load redistribution of RC frames subjected to the loss of a corner column scenario. The Vierendeel action
273 could resist the collapse of the buildings. For simplicity, due to the Vierendeel action, bending moment
274 may develop in the beam end near the corner column to help the resistance of collapse.

275 Fig. 20 demonstrates the comparison of load resistance between single-story and two-story moment
276 frames under both CL and UDL methods. The peak load of US-CL-1F, US-CL-2F, US-UDL-1F, and
277 US-UDL-2F are 43.7 kN, 250.6 kN, 141.9 kN, and 525.2 kN, respectively. Thus, for CL method, the
278 peak load of US-CL-2F is 324 % of that of US-CL-1F, which is much greater than the theoretical value
279 of 200 %. The relatively large discrepancy could be attributed to Vierendeel action developed in US-
280 CL-2F. For US-CL-1F, no Vierendeel action could be developed as the constraints from structural
281 components in the upper story are ignored. However, the peak load of US-UDL-2F is 210 % of that of
282 US-UDL-1F. Thus, comparing to CL method, the effects of Vierendeel action are quite limited. As
283 mentioned above, the effects of Vierendeel action are expressed by developing positive moment at the
284 beam end near the corner column. Thus, the mobilization of Vierendeel action may be reflected
285 indirectly by the magnitude of shear force developed in the corner column. As shown in Fig. 21, much
286 greater shear force develops in the corner column of US-CL-2F, comparing to US-UDL-2F.

287 4.2. Structural resistance from each story

288 Fig. 22 shows the comparison of the load resistance from different stories of a two-story frame with
289 that from a single-story substructure. As shown in the figure, the load resistance of each story is different
290 after the elastic stage. For CL method, compared with the single-story frame, the peak load of the first

291 and second stories increases by 79 % and 58 %, respectively. However, under the UDL condition, the
292 peak load of the first and second stories only increases by 7 % and 3 %, respectively. For both loading
293 approaches, the bottom story achieves the greater load resisting capacity, which indicates that the
294 Vierendeel action is more efficient in the bottom story, as the structural components in the second story
295 could provide more significant constraints to the corner joint in the bottom story.

296 **4.3. Load transfer mechanisms of multi-story RC frames**

297 As aforementioned, the load transfer mechanisms in each story of the two-story frame are different.
298 Thus, it is necessary to investigate load transfer mechanisms developing in each story of multi-story
299 frames. Note that US-CL-3F, US-CL-4F, and US-CL-5F represent three-story, four-story, and five-story
300 frame substructures under CL case, respectively. Similarly, US-UDL-3F and US-UDL-4F represent
301 three-story and four-story frame substructures under the UDL case.

302 **4.3.1. Structural resistance of multi-story frames**

303 For US-CL-3F, US-CL-4F, and US-CL-5F, as shown in Fig. 23 (a), (b), and (c), the structural
304 resistance developing in each story is different. The maximum load resistance is observed in the first
305 story, which is the same as that found in US-CL-2F. By increasing the number of stories, it can be found
306 that the initial stiffness, peak load, and residual load resistance of the middle story are pretty similar,
307 which indicates that the development of load transfer mechanisms of the middle stories is almost
308 identical. Moreover, the peak load of the middle stories is the least compared with the top and bottom
309 ones. Like the CL case, for US-UDL-3F and US-UDL-4F, as shown in Fig. 24 (a) and (b), the bottom
310 story also achieves the most significant initial stiffness and peak load. However, the difference of load
311 resistance between the top story and the middle story is quite limited due to less Vierendeel action

312 developed in UDL cases. In addition, due to the weak tie force from the surrounding elements, less TCA
313 and TMA could be mobilized to resist progressive collapse under both CL and UDL methods. As shown
314 in Fig. 23, comparing the load-displacement curve of the first story in models of US-CL-3F, US-CL-4F,
315 and US-CL-5F shows that increasing the story number will not affect the load resistance and load transfer
316 mechanisms of the first story. In other words, the constraints to the corner joint in the first story are
317 similar whatever the story number is three, four, or five.

318 **4.3.2. Axial force of beams in multi-story frames**

319 Similar to what was discussed in section 3.3, the results of axial force in beams were also extracted
320 to illustrate the load transfer mechanisms. For simplicity, only the cross-sections of beam AB were
321 discussed herein. Note that the label of X-beam-1 to X-beam-5 represents the beams in the first to the
322 fifth story, respectively.

323 As shown in Fig. 25, for CL case, the beams in each story are in compression before the
324 displacement of 300 mm. After that, the axial force starts to decrease and changes into tension
325 successively. Moreover, the beams in the first story begin to develop the CAA initially and achieve the
326 maximum compressive force of 209.6 kN at the displacement of 112 mm. By contrast, beams in the top
327 story achieve the maximum compressive force of 128.7 kN at the displacement of 214 mm, which
328 indicates lower CAA developed in top story. Moreover, the compressive force is the least in the middle
329 story compared with the top and first stories. Similarly, for UDL case, as shown in Fig. 26, the largest
330 compressive force of 106.3 kN is measured in the first story. Moreover, the compressive force in the
331 beams in the top story is slightly larger than that in the middle story.

332 For both loading methods, it is observed that the axial force of beams in the middle stories is similar,
333 which agrees well with the results of load resistance.

334 5. Conclusions

335 Based on the numerical and parametric study conducted in this study, the following conclusions are
336 drawn:

337 1. Compared with experimental results, it is found that the high-fidelity numerical models can simulate
338 the global behavior of the RC beam-slab substructure subjected to a corner column loss scenario well.
339 However, the shear fracture energy should be adjusted to well simulate the stiffness of the concrete in
340 CSCM.

341 2. For single-story models under either UDL or CL methods: US-UDL-1F and US-CL-1F, the peak
342 load of US-UDL-1F is 537 % of that US-CL-1F, which is greater than the theoretical value of 400%.
343 Thus, it indicates that the simplified CL method may underestimate the load resistance of the beam-slab
344 substructures subjected to the loss of a corner column scenario. It could be explained as UDL method
345 may achieve more uniform deformation of the beam and slab, and thus, more materials could be fully
346 mobilized.

347 3. For multi-story models, it was found that Vierendeel action could not be ignored to resist
348 progressive collapse of RC frames caused by the loss of a corner column scenario. Comparing to multi-
349 story frames subjected to UDL method, the Vierendeel action has more significant effects on the frames
350 under CL method. As the building was subjected to UDL load, in reality, the commonly used CL method
351 may overestimate the contribution of Vierendeel action. Moreover, the Vierendeel action is more
352 efficient in lower stories than that in the upper stories. Therefore, in practical design, it was suggested
353 to apply UDL load and generating multi-story frames to obtain more accurate results.

354 4. The numerical results indicated that the load transfer mechanisms developed in different stories are

355 not identical for a multi-story frame subjected to the loss of a corner column scenario. Moreover, it was
356 found that increasing the story number will not affect the load resistance and load transfer mechanism
357 of the first story.

358 **References**

- 359 [1] ASCE/SEI 7, Recommendations for Designing Collapse-Resistant Structures, Structural
360 Engineering Institute-American Society of Civil Engineers, Reston, VA, 2010.
- 361 [2] GSA, Progressive Collapse Analysis and Design Guidelines for New Federal Office Buildings and
362 Major Modernization Projects, U.S. General Service Administration, Washington, DC, 2003.
- 363 [3] Department of Defense (DoD), Design of Building to Resist Progressive Collapse. Unified Facility
364 Criteria, UFC 4-023-03, US Department of Defense, Washington (DC), 2009.
- 365 [4] Y. Zhou, T.P. Chen, Y.L. Pei, H.J. Hwang, X. Hu, W.J. Yi, L. Deng, Static load test on progressive
366 collapse resistance of fully assembled precast concrete frame structure, Eng. Struct. 200 (2019) 109719.
- 367 [5] P. Feng, H.L. Qiang, X. Ou, W.H. Qin, J.X. Yang, Progressive collapse resistance of GFRP-
368 strengthened RC beam–slab subassemblages in a corner column–removal scenario, J. Compos. Constr.
369 23 (2018) 04018076.
- 370 [6] M. Sasani, Response of a reinforced concrete infilled-frame structure to removal of two adjacent
371 columns, Eng. Struct. 30(9) (2008) 2478-2491.
- 372 [7] K. Qian, S.L. Liang, F. Fu, Y. Li, Progressive collapse resistance of emulative precast concrete
373 frames with various reinforcing details, J. Struct. Eng. 147(8) (2021) 04021107.
- 374 [8] X.F. Deng, S.L. Liang, F. Fu, K. Qian, Effects of high-strength concrete on progressive collapse
375 resistance of reinforced concrete frame, J. Struct. Eng. 146(6) (2020) 04020078.
- 376 [9] X.Z. Lu, K.Q. Lin, Y. Li, H. Guan, P.Q. Ren, Y.L. Zhou, Experimental investigation of RC beam-

377 slab substructures against progressive collapse subject to an edge-column-removal scenario, *Eng. Struct.*
378 149 (2017) 91-103.

379 [10]P.Q. Ren, Y. Li, X.Z. Lu, H. Guan, Y.L. Zhou, Experimental investigation of progressive collapse
380 resistance of one-way reinforced concrete beam-slab substructures under a middle-column-removal
381 scenario, *Eng. Struct.* 118 (2016) 28-40.

382 [11]N.S. Lim, K.H. Tan, C.K. Lee, Experimental studies of 3D RC substructures under exterior and
383 corner column removal scenarios, *Eng. Struct.* 150 (2017) 409–427.

384 [12]A.T. Pham, N.S. Lim, K.H. Tan, Investigations of tensile membrane action in beam-slab systems
385 under progressive collapse subject to different loading configurations and boundary conditions, *Eng.*
386 *Struct.* 150 (2017) 520–536.

387 [13]K. Qian, B. Li, Slab effects on response of reinforced concrete substructures after loss of corner
388 column, *ACI Struct. J.* 109 (6) (2012) 845–855.

389 [14]K. Qian, B. Li, J.X. Ma, Load-carrying mechanism to resist progressive collapse of RC buildings,
390 *J. Struct. Eng.* 141(2) (2015) 04014107.

391 [15]K. Qian, B. Li, Z. Zhang, Influence of multicolumn removal on the behavior of RC floors, *J. Struct.*
392 *Eng.* 142 (5) (2016), 04016006.

393 [16]K. Qian, B. Li, Load-resisting mechanism to mitigate progressive collapse of flat slab structures,
394 *Mag. Concr. Res.* 67 (7) (2015) 349–363.

395 [17]P.X. Pham, K.H. Tan, Experimental response of beam-slab substructures subject to penultimate-
396 external column removal, *J. Struct. Eng.* 141(7) (2015) 04014107.

397 [18]X.D. Pham, K.H. Tan, Experimental study of beam–slab substructures subjected to a penultimate-
398 internal column loss, *Eng. Struct.* 55 (2013) 2–15.

- 399 [19]Y.H. Weng, K. Qian, F. Fu, Q. Fang, Numerical investigation on load redistribution capacity of flat
400 slab substructures to resist progressive collapse, *J. Build. Eng.* 29 (2020) 101109.
- 401 [20]K. Qian, Y.H. Weng, F. Fu, X.F. Deng, Numerical evaluation of the reliability of using single-story
402 substructures to study progressive collapse behaviour of multi-story RC frames, *J. Build. Eng.* 33 (2021)
403 101636.
- 404 [21]J. Yu, L. Luo, Y. Li, Numerical study of progressive collapse resistance of RC beam-slab
405 substructures under perimeter column removal scenarios, *Eng. Struct.* 159 (2018) 14-27.
- 406 [22]A.T. Pham, K.H. Tan, J. Yu, Numerical investigations on static and dynamic responses of reinforced
407 concrete sub-assemblages under progressive collapse, *Eng. Struct.* 149 (2017) 2-20.
- 408 [23]J. Yu, Y.P. Gan, J. Wu, H. Wu, Effect of concrete masonry infill walls on progressive collapse
409 performance of reinforced concrete infilled frames, *Eng. Struct.* 191 (2019) 179-193.
- 410 [24]Y. Li, X.Z. Lu, H. Guan, L.P. Ye, An improved tie force method for progressive collapse resistance
411 design of reinforced concrete frame structures. *Eng. Struct.* 33(10) (2011) 2931–2942.
- 412 [25]D.C. Feng, S.C. Xie, J. Xu, K. Qian, Robustness quantification of reinforced concrete structures
413 subjected to progressive collapse via the probability density evolution method, *Eng. Struct.* 202 (2020)
414 109877.
- 415 [26]Ministry of Housing and Urban-Rural Development of the People's Republic of China (MOHURD).
416 Code for design of concrete structures. GB50010-2010. Beijing, China; 2010.
- 417 [27]Ministry of Housing and Urban-Rural Development of the People's Republic of China (MOHURD).
418 Code for seismic design of buildings, GB50011-2010. Beijing, China; 2010.
- 419 [28]Y. Wu, J.E. Crawford, J.M. Magallanes, Performance of LS-DYNA concrete constitutive models,
420 12th Int. LS-DYNA Users Conf, Livermore Software Technology Corporation, Livermore, CA, 2012.

421 [29]J. Hallquist, LS-DYNA Keyword User's Manual, Version 971, Livermore Software Technology
422 Corp., Livermore, CA, 2007.

423 [30]CEB. CEB-FIP model code 1990. Thomas Telford; 1991.

424 [31]B.A Izzuddin, A.G Vlassis, A.Y Elghazouli, D.A Nethercot, Progressive collapse of multi-storey
425 buildings due to sudden column loss — Part I: Simplified assessment framework, Eng. Struct. 30(5)
426 (2008) 1309–18.

427

428 **Captions of tables**

429 **Table 1**-Reinforcement properties

430 **Table 2**-Study on different mesh sizes

431 **Table 3**-Model parameters of CSCM for FE models (Unit: N, mm and ms)

432 **Table 4**-Comparison of key results between test and FE model

433

434 **Captions of figures**

435 **Fig. 1**–Dimensions of specimen US (units: mm) [5]

436 **Fig. 2**–Test setup and instrumentation location in the referenced experiment [5]

437 **Fig. 3**–Numerical model of US-CL-1F

438 **Fig. 4**–Comparison of different mesh sizes

439 **Fig. 5**–General shape of concrete model yield surface

440 **Fig. 6**–Comparison of different concrete input parameters

441 **Fig. 7**–Unconfined uniaxial stress-strain curve of concrete based on CSCM

442 **Fig. 8**–Comparison of load-displacement curves between test and FE model

443 **Fig. 9**–Comparison of failure modes between test and FE model: (a) US [5]; (b) US-CL-1F

444 **Fig. 10**–Comparison of the crack distributions between test and FE model: (a) US [5]; (b) US-CL-1F

445 **Fig. 11**–Details of numerical model for load distribution rig

446 **Fig. 12**–Layout of the loading system (unit: mm)

447 **Fig. 13**–Numerical model of US-UDL-1F

448 **Fig. 14**–Comparison of load-displacement curves between US-CL-1F and US-UDL-1F

449 **Fig. 15**–Failure modes of the slab in model US-UDL-1F: (a) Top surface of the slab; (b) Bottom surface

450 of the slab

451 **Fig. 16**–Development of beam axial force: (a) US-CL-1F; (b) US-UDL-1F

452 **Fig. 17**–Contribution of each supporting column: (a) US-CL-1F; (b) US-UDL-1F

453 **Fig. 18**–Dynamic resistance of beam-slab substructures

454 **Fig. 19**–Numerical models: (a) US-CL-2F; (b) US-UDL-2F

455 **Fig. 20**–Comparison of load-displacement curves between CL and UDL conditions

456 **Fig. 21**–Development of shear force of corner column

457 **Fig. 22**–Comparison of load resistance from different stories with single-story substructure: (a) US-CL-

458 2F; (b) US-UDL-2F

459 **Fig. 23**–Load resistance of each story under CL: (a) US-CL-3F; (b) US-CL-4F; (c) US-CL-5F

460 **Fig. 24**–Load resistance of each story under UDL: (a) US-UDL-3F; (b) US-UDL-4F

461 **Fig. 25**–Beam axial force of each story under CL: (a) US-CL-3F; (b) US-CL-4F; (c) US-CL-5F

462 **Fig. 26**–Beam axial force of each story under UDL: (a) US-UDL-3F; (b) US-UDL-4F

463

464

Table 1-Reinforcement properties

Items	Diameter (mm)	Yield strength (MPa)	Ultimate strength (MPa)	Elongation (%)	Yield strain ($\mu\epsilon$)
R6	6	324	525	23	1543
T12	12	427	530	18	2135

465

Note: R6 represents plain bar with diameter of 6 mm; T12 represents deformed rebar with diameter of 12 mm.

466

Table 2-Study on different mesh sizes

Type	Mesh size 1	Mesh size 2	Mesh size 3
Mesh size of slabs (mm)	25×25×23.3	20×20×17.5	20×20×14
Mesh size of beams and columns (mm)	25×25×25	20×20×20	15×15×15
Mesh size of Reinforcements (mm)	25	20	15
Total number of solid elements	76672	152325	367990
Total number of beam elements	23330	29210	38708
Time consuming (s)	36241	43717	144940

467

Table 3-Model parameters of CSCM for FE models (Unit: N, mm and ms)

MID	RO	NPLOT	INCRE	IRATE	ERODE	RECOV	ITRETRE
1	0.00232	1	0.0	0	1.10	0.0	0
PRED							
0.0							
G	K	ALPHA	THETA	LAMDA	BETA	HN	CH
5000	5476	13.408	0.2751	10.5	0.01929	0.0	0.0
ALPHA1	THETA1	LAMDA1	BETA1	ALPHA2	THETA2	LAMDA2	BETA2
0.74735	0.001315	0.17	0.07639	0.66	0.001581	0.16	0.07639
R	XD	W	D1	D2			
5.0	87.8	0.05	2.5e-4	3.492e-7			
B	GFC	D	GFT	GFS	PWRC	PWRT	PMOD
100.0	3.308	0.1	0.06616	0.03308	5.0	1.0	0.0
ETA0C	NC	ETAOT	NT	OVERC	OVERT	SRATE	REP0W
0.0	0.0	0.0	0.0	0.0	0.0	0.0	0.0

468

Table 4-Comparison of key results between test and FE model

Results Source	Critical Displacement (mm)		Critical Load (kN)		
	YL	PL	YL	PL	UL
Test	50	85.2	35	43.5	14.1
FEM	46.8	83.6	37.1	43.7	13.6
FEM/Test	0.936	0.981	1.06	1.005	0.965

469

Note: YL, PL, and UL represent yield load, peak load, and ultimate load, respectively.

470

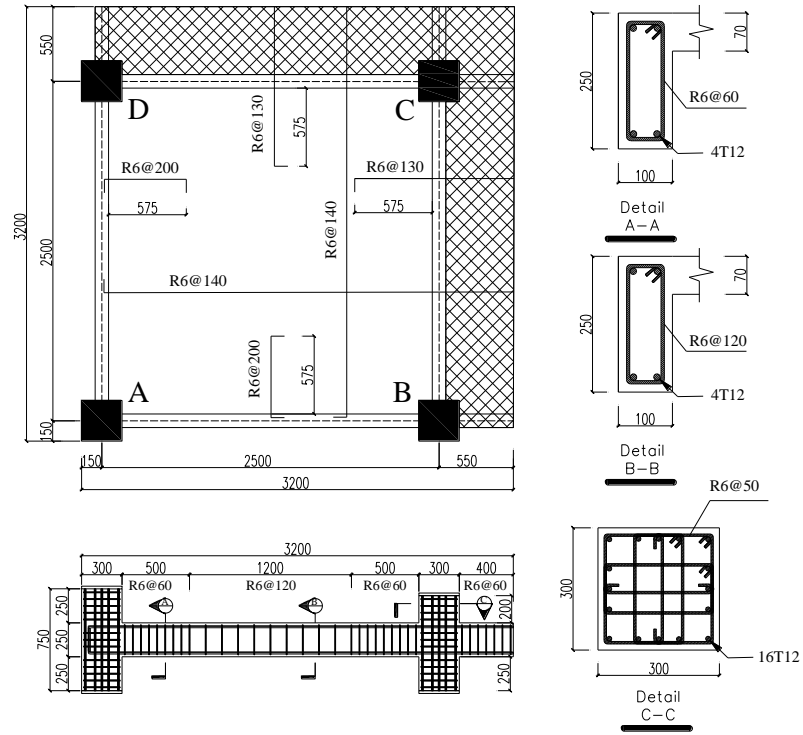


Fig. 1 Dimensions of Specimen US (units: mm) [5]

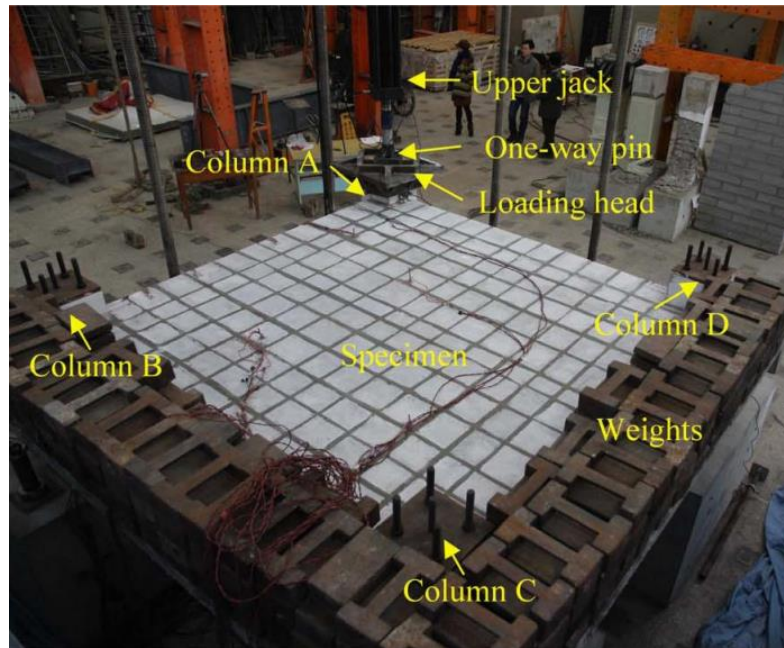
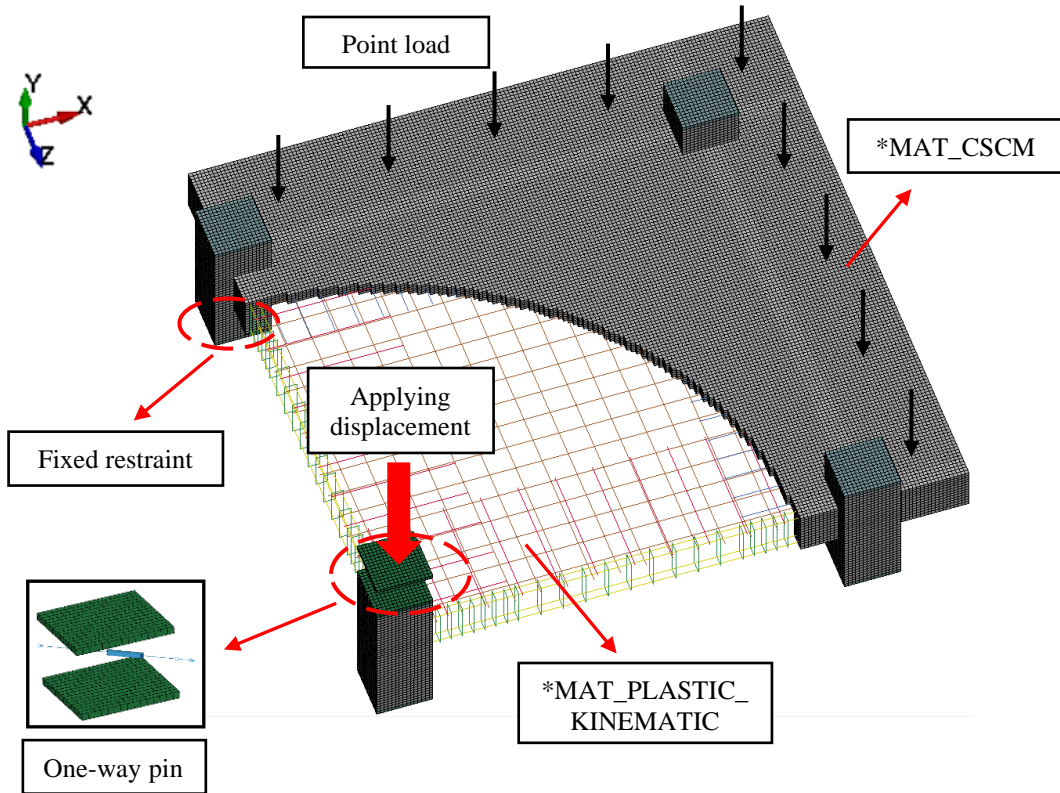


Fig. 2 Test setup and instrumentation location in the referenced experiment [5]

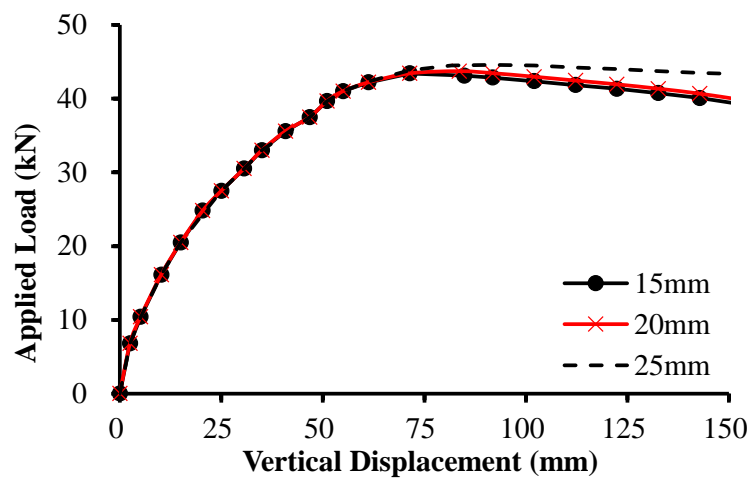


477

478

479

Fig. 3 Numerical model of US-CL-1F



480

481

Fig. 4 Comparison of different mesh sizes

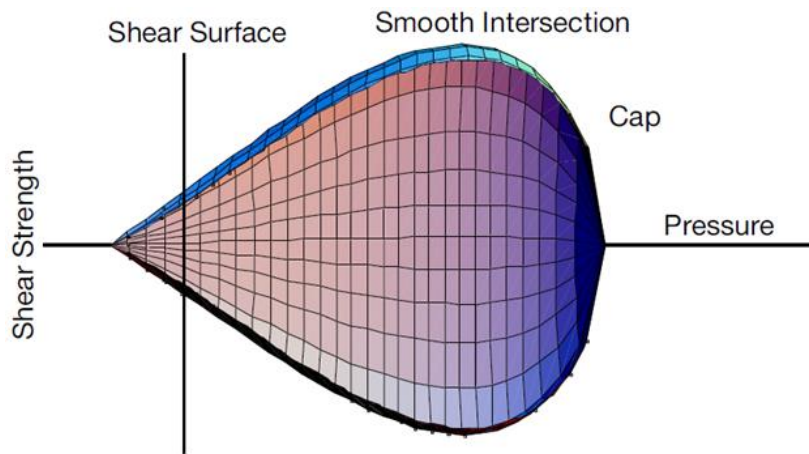


Fig. 5 General shape of concrete model yield surface

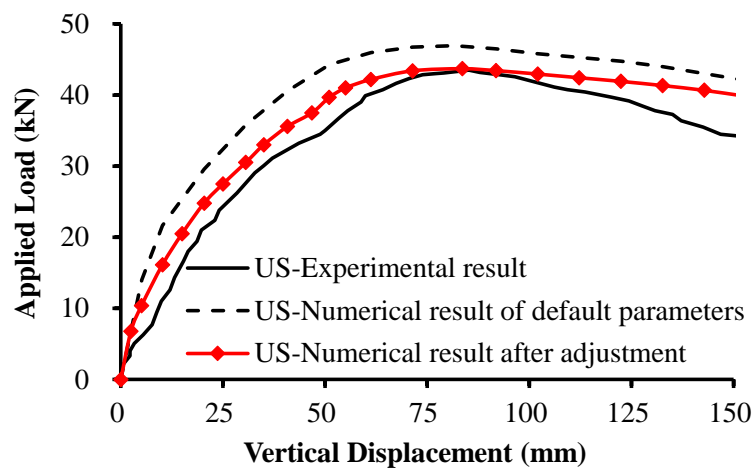
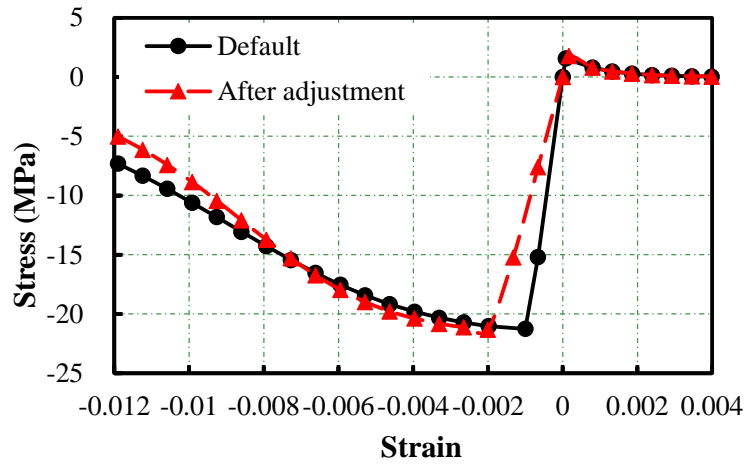


Fig. 6 Comparison of different concrete input parameters



492

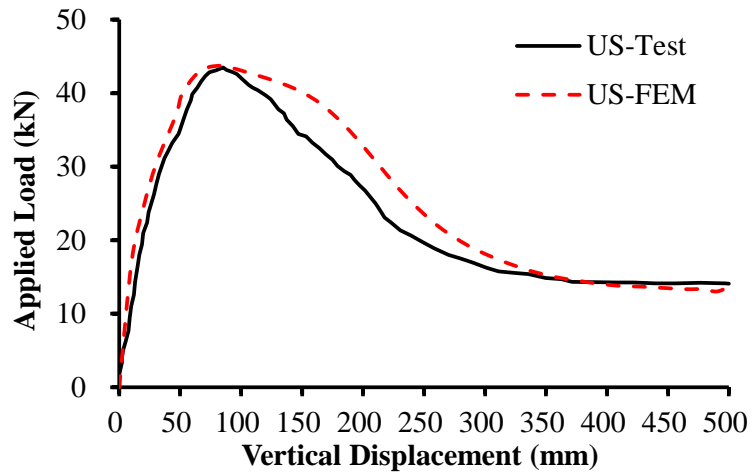
493

Fig. 7 Unconfined uniaxial stress-strain curve of concrete based on CSCM

494

495

496

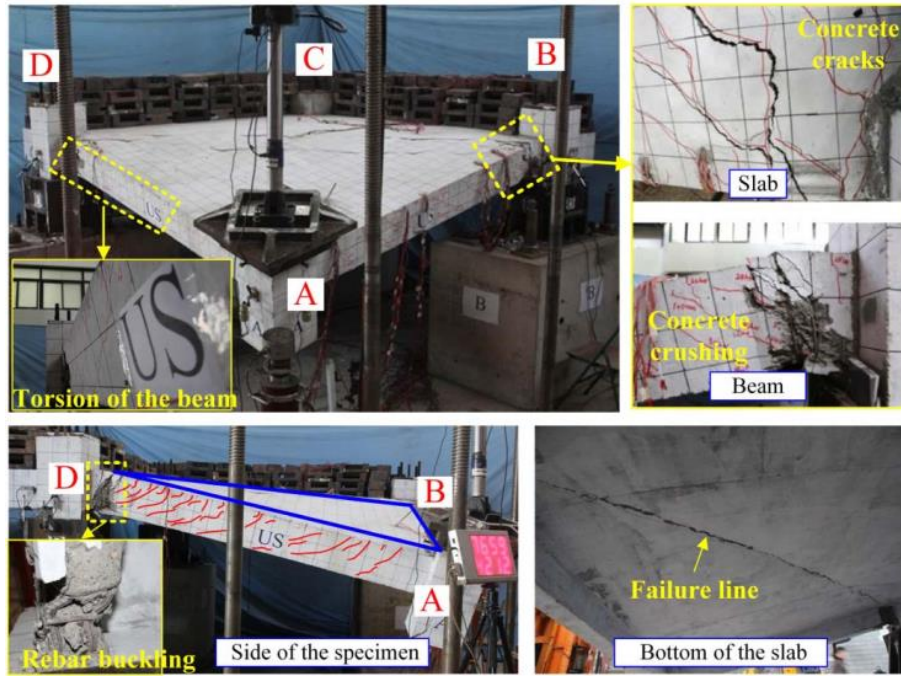


497

498

Fig. 8 Comparison of load-displacement curves between test and FE model

499



(a)



(b)

Fig. 9 Comparison of failure modes between test and FE model: (a) US [5]; (b) US-CL-1F

500

501

502

503

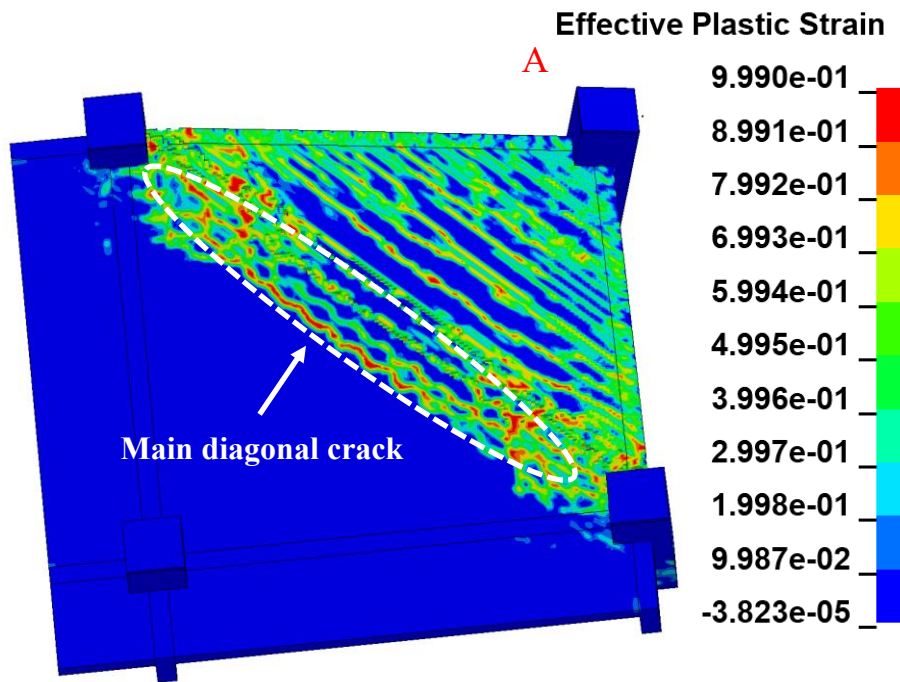
504

505



506
507

(a)

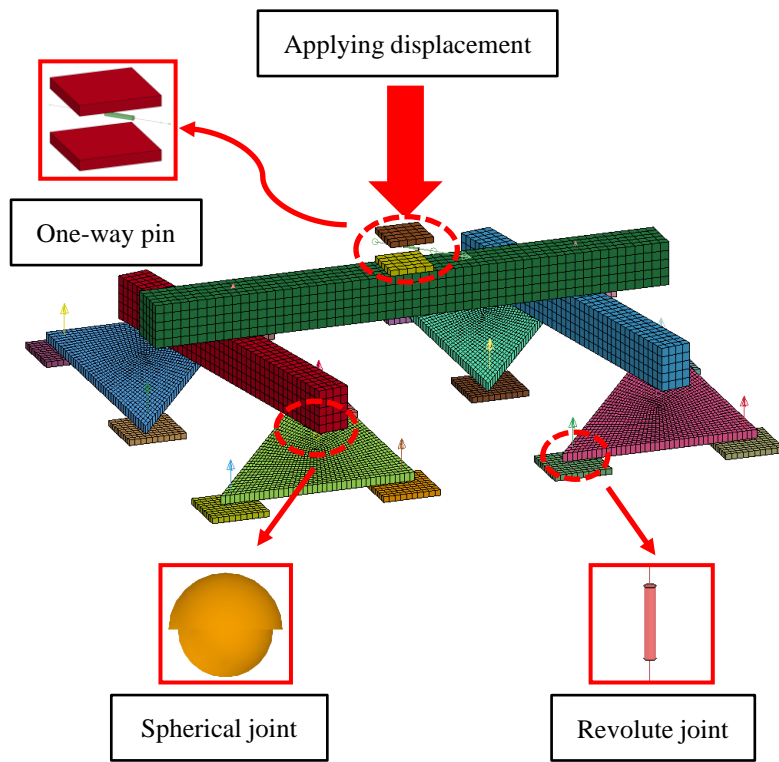


508
509

(b)

510 **Fig. 10** Comparison of the crack distributions between test and FE model: (a) US [5]; (b) US-CL-1F

511

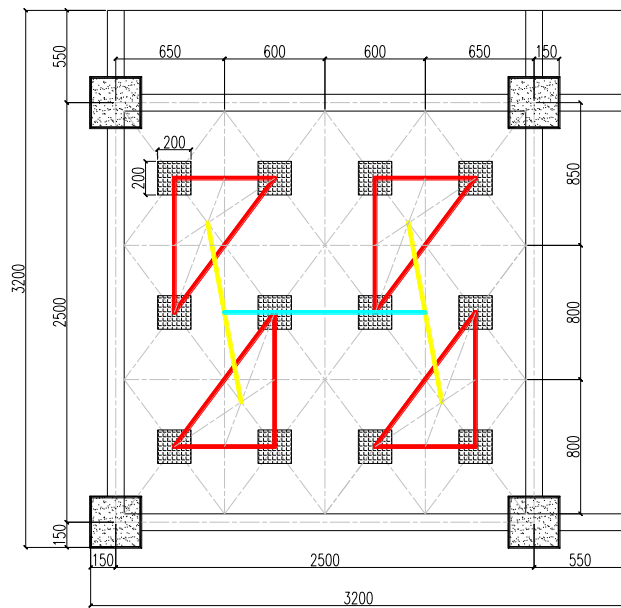


512

513

Fig. 11 Details of numerical model for load distribution rig

514

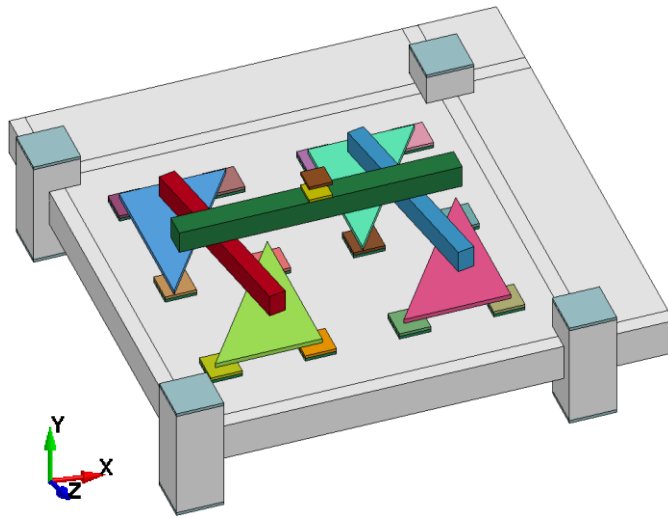


515

516

Fig. 12 Layout of the loading system (unit: mm)

517

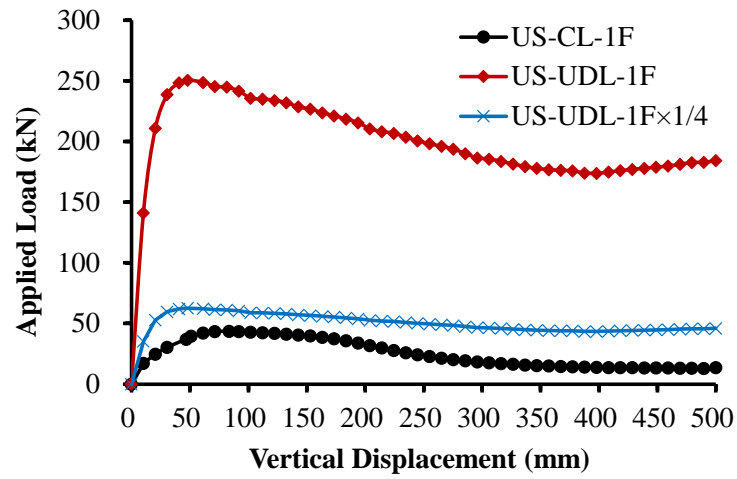


518

519

Fig. 13 Numerical model of US-UDL-1F

520

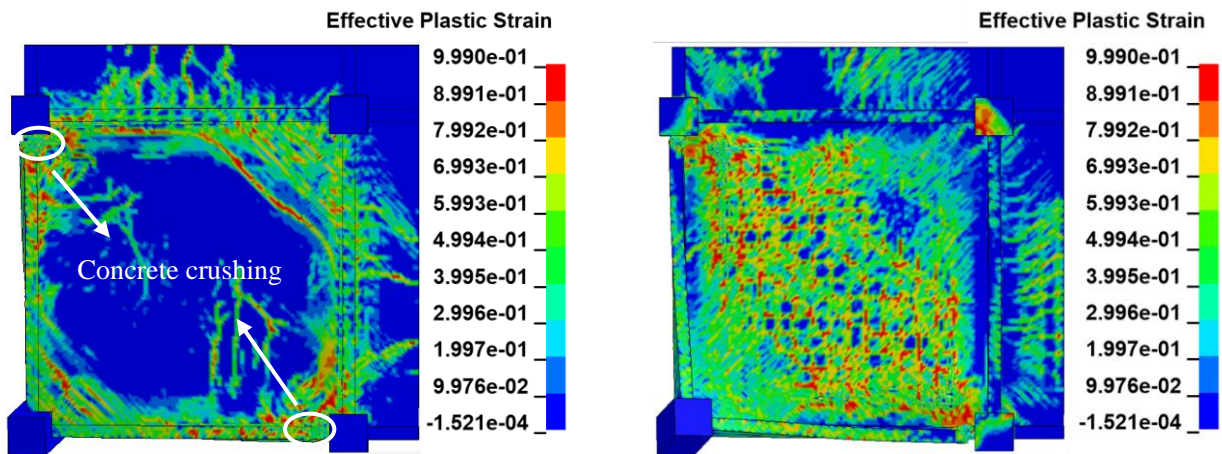


521

522

Fig. 14 Comparison of load-displacement curves between US-CL-1F and US-UDL-1F

523



524

525

(a)

(b)

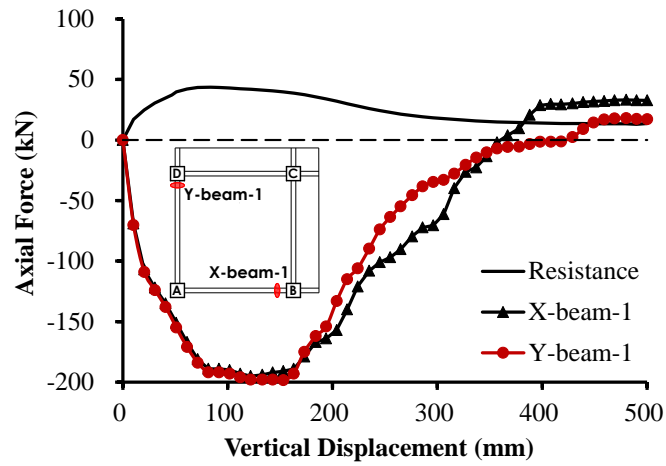
526

Fig. 15 Failure modes of the slab in model US-UDL-1F: (a) Top surface of the slab; (b) Bottom

527

surface of the slab

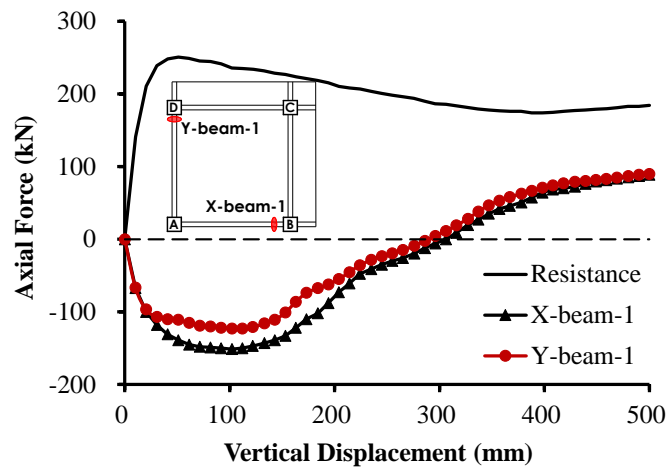
528



529

530

(a)



531

532

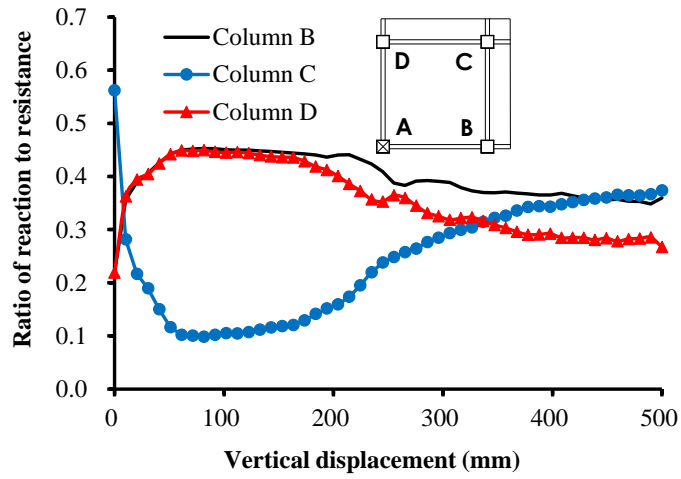
(b)

533

Fig. 16 Development of beam axial force: (a) US-CL-1F; (b) US-UDL-1F

534

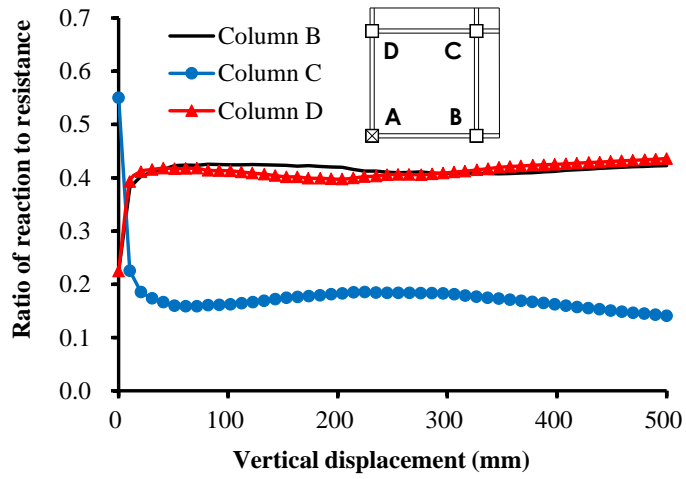
535



536

537

(a)



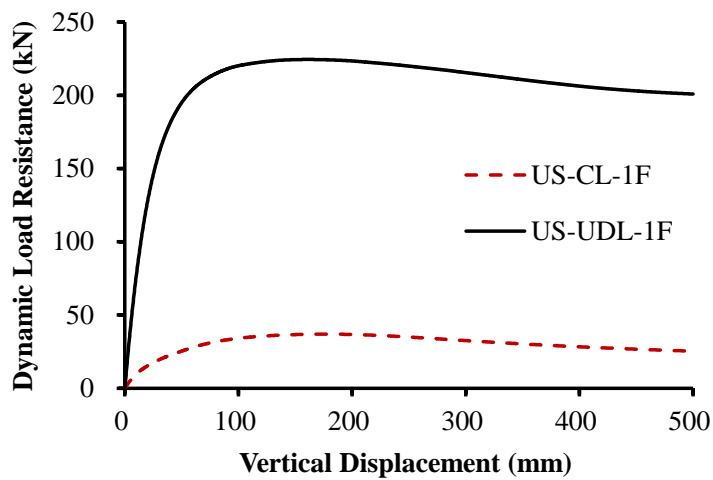
538

539

(b)

540

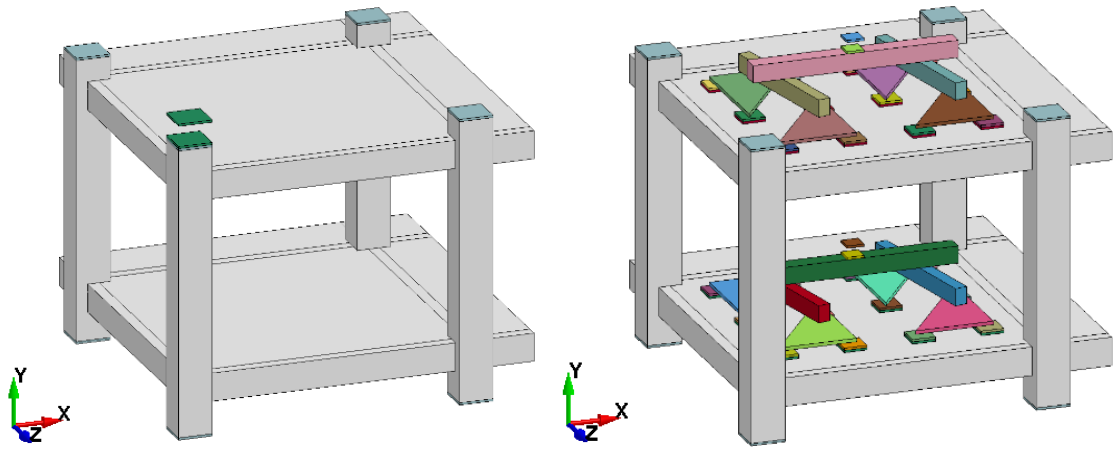
Fig. 17 Contribution of each supporting column: (a) US-CL-1F; (b) US-UDL-1F



541

542

Fig. 18 Dynamic resistance of beam-slab substructures



(a)

(b)

Fig. 19 Numerical models: (a) US-CL-2F; (b) US-UDL-2F

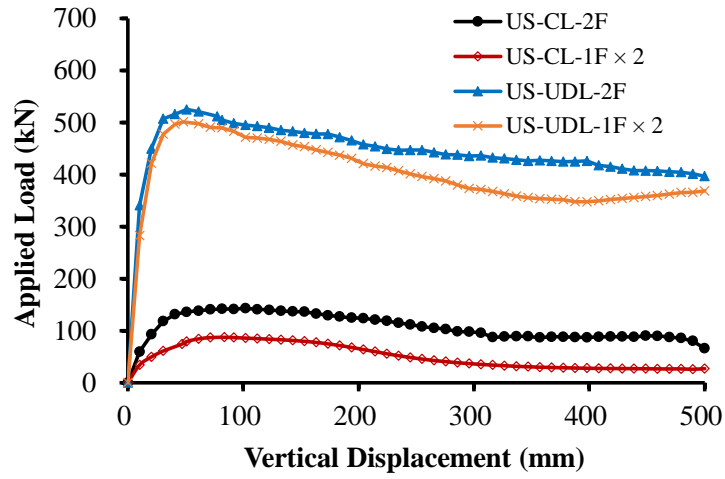


Fig. 20 Comparison of load-displacement curves between CL and UDL conditions

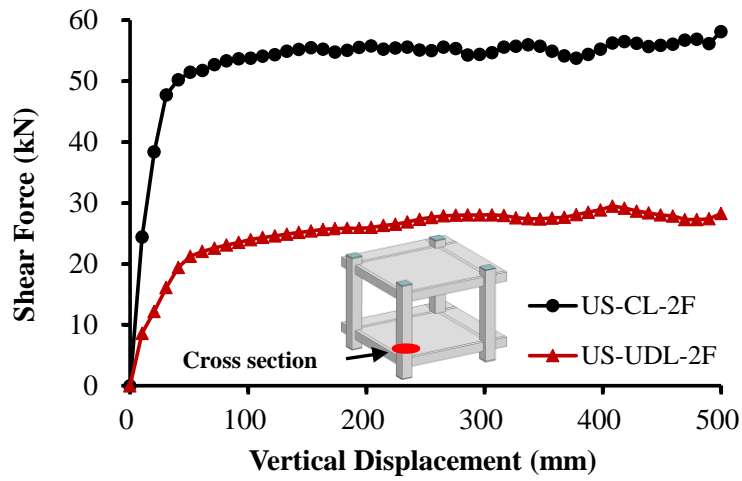
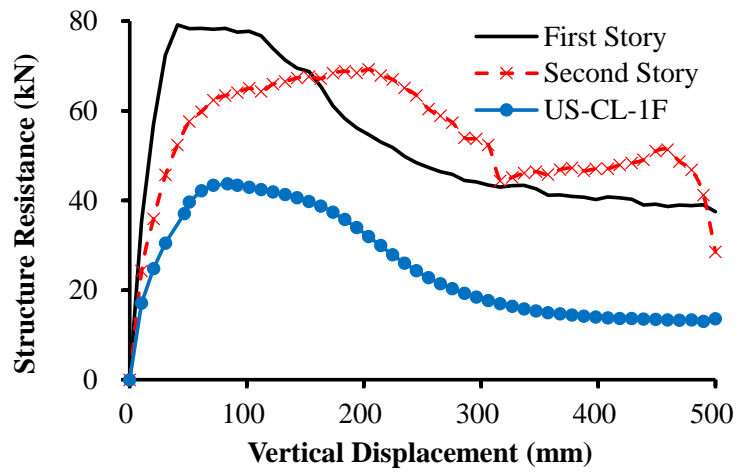


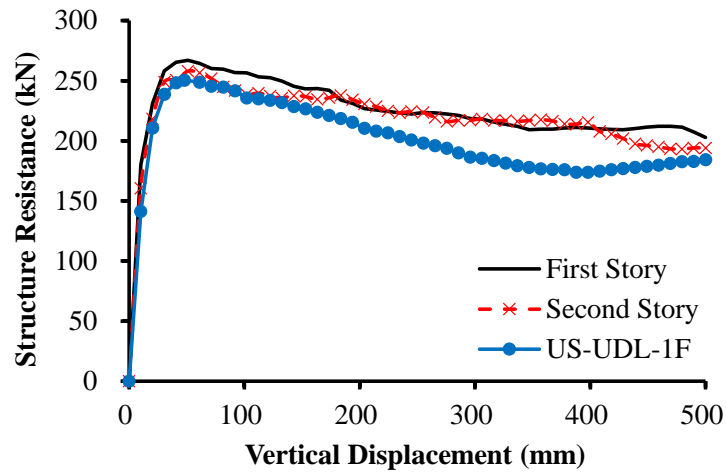
Fig. 21 Development of shear force of corner column



550

551

(a)



552

553

(b)

554

Fig. 22 Comparison of load resistance from different stories with single-story substructure:

555

(a) US-CL-2F; (b) US-UDL-2F

556

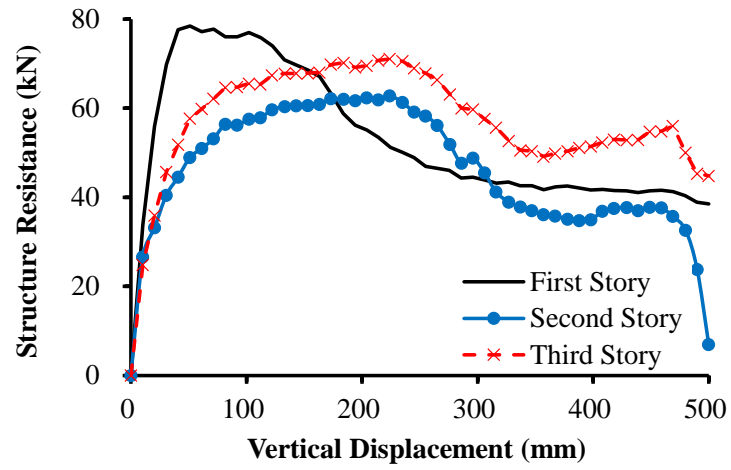
557

558

559

560

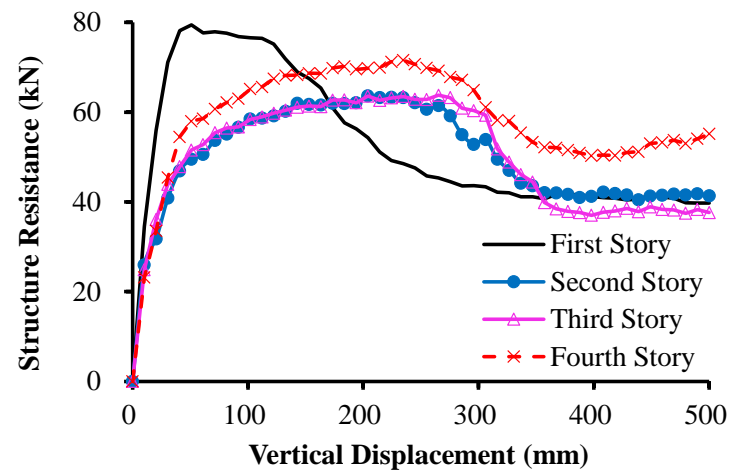
561



562

563

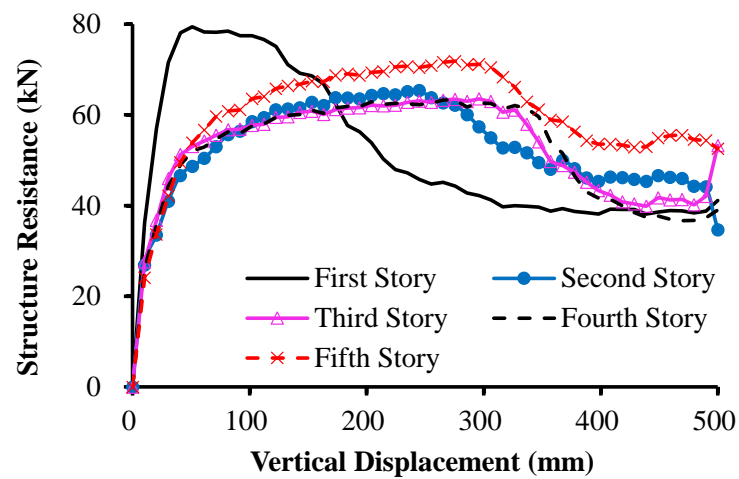
(a)



564

565

(b)



566

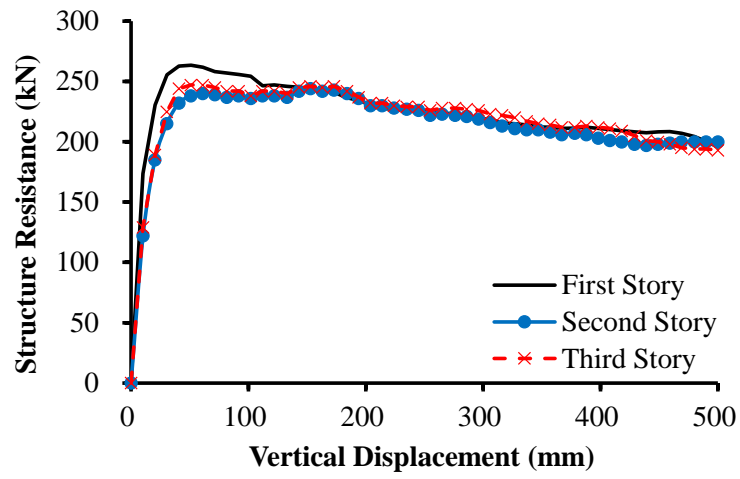
567

(c)

568

Fig. 23 Load resistance of each story under CL: (a) US-CL-3F; (b) US-CL-4F; (c) US-CL-5F

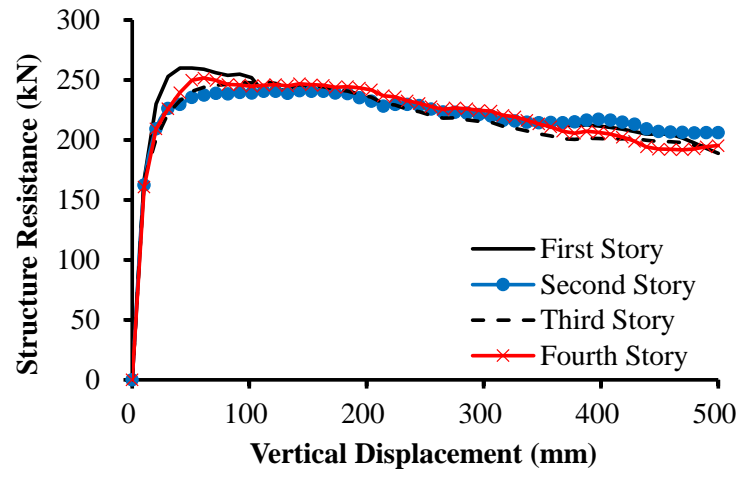
569



570

571

(a)



572

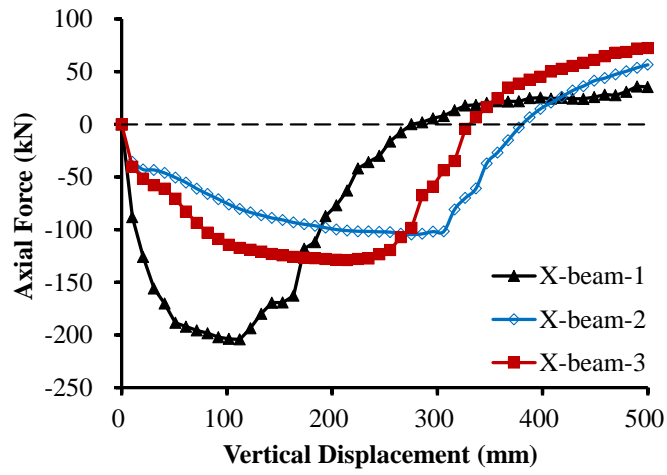
573

(b)

574

Fig. 24 Load resistance of each story under UDL: (a) US-UDL-3F; (b) US-UDL-4F

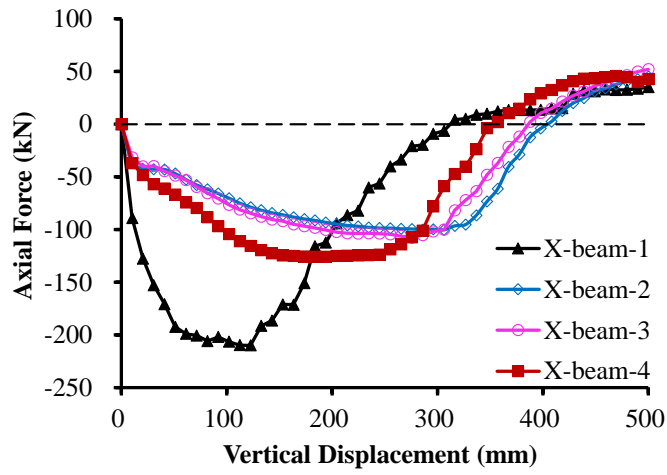
575



576

577

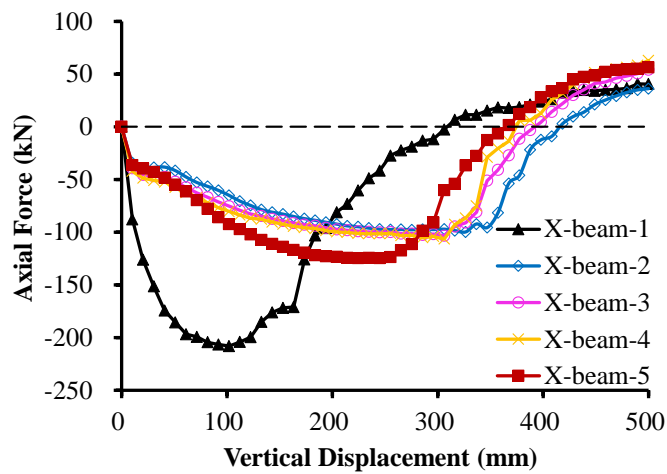
(a)



578

579

(b)



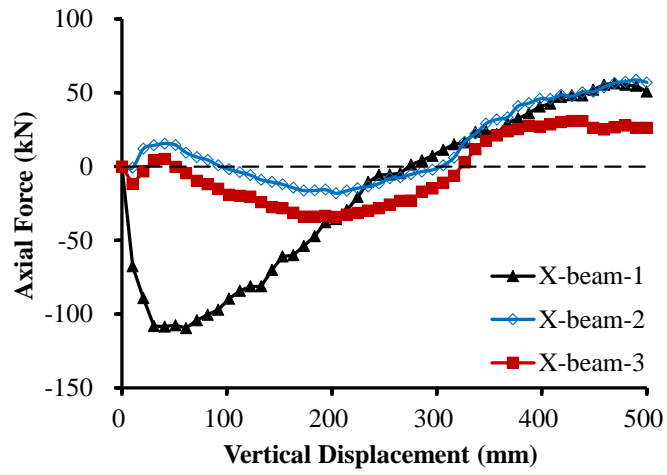
580

581

(c)

582

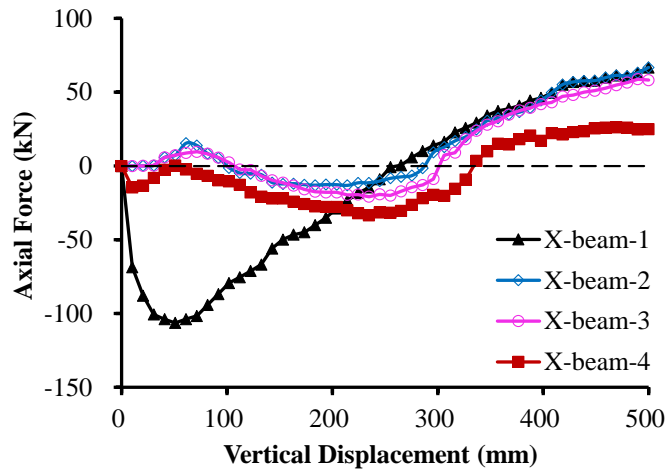
Fig. 25 Beam axial force of each story under CL: (a) US-CL-3F; (b) US-CL-4F; (c) US-CL-5F



583

584

(a)



585

586

(b)

587

Fig. 26 Beam axial force of each story under UDL: (a) US-UDL-3F; (b) US-UDL-4F